

## Full length article

## Screening of generalized stacking fault energies, surface energies and intrinsic ductile potency of refractory multicomponent alloys

Yong-Jie Hu<sup>a,b</sup>, Aditya Sundar<sup>a</sup>, Shigenobu Ogata<sup>c</sup>, Liang Qi<sup>a,\*</sup><sup>a</sup> Department of Materials Science and Engineering, University of Michigan, Ann Arbor 48109, USA<sup>b</sup> Department of Materials Science and Engineering, Drexel University, Philadelphia 19104, USA<sup>c</sup> Department of Mechanical Science and Bioengineering, Osaka University, Osaka 560-8531, Japan

## ARTICLE INFO

## Article history:

Received 9 August 2020

Revised 28 February 2021

Accepted 7 March 2021

Available online 18 March 2021

## ABSTRACT

Body-centered cubic (bcc) refractory multicomponent alloys are of great interest due to their remarkable strength at high temperatures. Optimizing the chemical compositions of these alloys to achieve a combination of high strength and room-temperature ductility remains challenging. Systematic predictions of these correlated properties across a vast compositional space would speed the alloy discovery process. In the present work, we performed first-principles calculations with the special quasi-random structure (SQS) method to predict the unstable stacking fault energy ( $\gamma_{\text{usf}}$ ) of the (110)[111] slip system and the (110)-plane surface energy ( $\gamma_{\text{surf}}$ ) for 106 individual binary, ternary and quaternary bcc solid-solution alloys with constituent elements among Ti, Zr, Hf, V, Nb, Ta, Mo, W, Re and Ru. Moreover, with the first-principles data and a set of physics-informed descriptors, we developed surrogate models based on statistical regression to accurately and efficiently predict  $\gamma_{\text{usf}}$  and  $\gamma_{\text{surf}}$  for refractory multicomponent alloys in the 10-element compositional space. Building upon binary and ternary data, the surrogate models show outstanding predictive capability in the high-order multicomponent systems. The ratio between  $\gamma_{\text{surf}}$  and  $\gamma_{\text{usf}}$  can be used to populate a model of intrinsic ductility based on the Rice model of crack-tip deformation. Therefore, using the surrogate models, we performed a systematic screening of  $\gamma_{\text{usf}}$ ,  $\gamma_{\text{surf}}$  and their ratio over 112,378 alloy compositions to search for alloy candidates that may have enhanced strength-ductility synergies. Search results were also validated by additional first-principles calculations.

© 2021 Acta Materialia Inc. Published by Elsevier Ltd. All rights reserved.

## 1. Introduction

Metals and alloys based on transition metal elements of Group V and VI in the periodic table (such as Nb, Ta, Mo, and W) usually have nearly half-filled d-band electrons. These electrons generate strong interatomic bonds with considerable directional dependence, and they make these alloys have the non-close packed bcc lattice structure [1]. Because of these electronic and atomistic structures, these alloys have high melting temperatures, and the dislocation motions in these alloys have more substantial activation barriers and temperature-dependent behavior compared with many other metallic alloys [2–6]. While these alloys (so-called refractory metals and alloys) can have excellent mechanical performances with high strengths and sufficient ductility at high temperatures (>1000 °C), but many are brittle at the room temperature, significantly limiting their mechanical processing and engineering applications.

Recently, there are developments of multicomponent alloys based on Group IV, V and VI elements mixed in either equimolar and non-equimolar ratios [7–12]. Some of these refractory high-entropy alloys (HEAs) were reported to have excellent mechanical performances in both strengths and ductility in extremely high-temperature regions [7,8,13–17]. However, these alloys generally have low ductility at room temperatures [8,18]. Because there are many degrees of freedom in the compositional space, it is urgent to develop efficient and accurate methods to predict the strengths and ductility of candidate alloys with arbitrary chemical compositions in order to search for alloys with optimized mechanical performances. So far, there have been many studies to predict the strengths of multicomponent HEA in both face-centered cubic (fcc) and bcc lattice structures [19–25]. However, only sparse theoretical studies were conducted to investigate their ductility, especially for bcc HEAs [15,26,117].

The evaluations of the ductility for general solid solution alloys using first-principles calculations are often conducted based on several well-established criteria. They include the Pugh's modulus ratio of the bulk and shear modulus of alloys [27], the lat-

\* Corresponding author.

E-mail address: [qiliang@umich.edu](mailto:qiliang@umich.edu) (L. Qi).

tice instability mechanism under ideal strength deformation [28–30], and the Rice criterion based on the competition between dislocation emissions and cleavage fracture propagation [31,32]. Using the linear elastic fracture mechanics (LEFM) analyses, the critical stress intensity factor for cleavage fracture propagation near a crack tip can be predicted by using elastic constants ( $c_{ij}$ ) and surface energies ( $\gamma_{\text{surf}}$ ) of cleavage planes, and the critical stress intensity factor for dislocation emissions near the crack tip can be predicted by using elastic constants and unstable stacking fault (USF) energies ( $\gamma_{\text{usf}}$ ) of specific slip systems. The intrinsic ductility of an alloy can be determined based on the ratio between these two types of stress intensity factors. Approximately, an alloy with a higher ratio of  $\frac{\gamma_{\text{surf}}}{\gamma_{\text{usf}}}$  can be considered to have a higher likelihood of being intrinsically ductile [26,31–34,117]. These approaches have been applied using either empirical interatomic potentials or first-principles calculations for different metals and alloys [26,34–36], including bcc HEAs [26,117].

However, to calculate these parameters ( $c_{ij}$ ,  $\gamma_{\text{surf}}$  and  $\gamma_{\text{usf}}$ ) of multicomponent solid-solution alloys based on first-principles calculations are not straightforward tasks. These calculations were often conducted using the relatively large supercells generated by the special quasi-random structure (SQS) method [37], which tunes the correlation functions of lattice occupations in the finite-size supercells to be close to those of the ideally mixed solid solutions. Multiple first-principles density functional theory (DFT) calculations have to be conducted to obtain the average results of the parameters for a specific alloy composition [38–42]. These expensive calculations limit our ability to explore compositional spaces efficiently.

Statistical learning methods can be applied to construct surrogate models to predict the parameters of HEAs and other multicomponent solid-solution alloys with DFT-level accuracies. However, a key bottleneck of these surrogate models is the small size of training data sets intrinsically limited by the costs of DFT calculations, which can undermine their extrapolative prediction ability. This limitation could be relieved by including the physical mechanisms in the surrogate model. As discussed above, the atomistic and electronic structures are strongly correlated to the deformation defect properties and the corresponding mechanical behavior of bcc transition-metal alloys. For example, the bcc alloys based on Group V elements are generally ductile, but those based on Group VI elements are generally brittle, although the latter have higher strengths, and these variations are controlled by the average filling level of d-band electrons [28,29]. Our recent studies also reveal the stability of deformation defects in bcc transition-metal alloys are strongly correlated to the features of local d-band shape and filling level [43]. Thus, it is possible to combine statistical regression methods and feature parameters of electronic and atomistic structures to construct an accurate and reliable model for bcc solid-solution alloys.

In this paper, we developed surrogate models based on statistical regression to learn the DFT calculations of USF energies ( $\gamma_{\text{usf}}$ ) and surface energies ( $\gamma_{\text{surf}}$ ) of {110} plane in multicomponent bcc solid-solution alloys mainly composed of Group IV, V, and VI elements. Based on a set of descriptors for capturing the features of atomic bonds and electronic structures of pure metals and ordered intermetallic alloys, our models can successfully predict the variations of USF and surface energies with an error of approximately 0.047 and 0.046 J/m<sup>2</sup>, respectively, in a large multicomponent space using only the chemical compositions as the inputs. Our current regression model trained only based on ~70 data of binary and ternary alloys can accurately predict  $\gamma_{\text{usf}}$  and  $\gamma_{\text{surf}}$  for quaternary alloys different from those in the training data. Using our surrogate models, we conducted a fast screening of  $\gamma_{\text{usf}}$  and  $\gamma_{\text{surf}}$  over a large number of quaternary bcc alloys, which are kinet-

ically possible to be synthesized based on the currently available phase diagrams [44]. The predictions of many extreme cases from these screening results were then confirmed by additional DFT calculations. The results suggest that their potency of strengths and ductility, which are related to  $\gamma_{\text{usf}}$  and  $\frac{\gamma_{\text{surf}}}{\gamma_{\text{usf}}}$ , respectively, are not solely determined by the d-band filling. In addition, there could be considerable spaces to tune alloy chemical compositions for further improvements of the strength-ductility synergy relative to the currently known equimolar HEAs.

We have to emphasize that several major approximations and simplifications have been taken in our framework. First, we only calculate the USF and surface energies without considering the composition effects on the elastic constants of alloys, which are needed to evaluate the critical stress intensity factors. Second, there could be multiple slip planes and fracture surface planes in bcc alloy systems besides {110} planes [45,46]. In principles, we can also predict these parameters based on the same framework of DFT calculations and statistical regression methods as discussed in this paper, but it would heavily increase our calculation efforts. Additionally, the elastic constants of solid-solution alloys can also be derived from recently developed machine learning models [47]. Other factors, such as the variations of local GSF [48–50], the effects of short-range ordering at 0 K and finite temperatures [49–53], and lattice-trapping effects on crack propagation [54,55], cannot be described by the average results of USF and surface energies from the first-principles calculations and the SQS method. Meanwhile, the contributions of other deformation mechanisms, such as deformation twinning, could be important to determine the strength and ductility of some specific HEAs [56–58], which can be further investigated in the future by applying the similar DFT methodologies [38,41,59]. Our strategy here is to develop these statistic regression models to efficiently search in the multicomponent compositional spaces to find the possible alloy compositions with optimized values of  $\gamma_{\text{usf}}$  and  $\frac{\gamma_{\text{surf}}}{\gamma_{\text{usf}}}$  under the assumption of ideally mixed solid-solution alloys. Once such candidates are identified, more rigorous calculations and defect models can be applied to evaluate their mechanical performances.

## 2. Methods

### 2.1. DFT calculations

#### 2.1.1. Computation of unstable stacking fault and surface energy

In the present work, the supercells for DFT calculations were built based on the special quasi-random structure (SQS) method [60] to approximately describe the chemical disorder in the studied solid-solution alloys. The SQSs were generated by using the Alloy Theoretic Automated Toolkit (ATAT) [37], in which a Monte Carlo-based evolutionary algorithm is used to search the periodic atomic structure with the closest match of correlation functions of a ideally mixed solid-solution state. Here, 13 types of SQSs were generated to study the bcc solid-solution phases with different binary, ternary and quaternary alloying compositions in a 10-element compositional space (i.e., Ti, Zr, Hf, V, Nb, Ta, Mo, W, Re and Ru). As listed in Table 1, 64 individual compositions were modeled for 14 binary systems, 10 compositions for 3 ternary systems, and 32 compositions for 12 quaternary systems.

Most of the generated SQSs are 72-atoms supercells are with orthogonal basis vectors, which are  $[1\bar{1}\bar{2}] \times 2[111] \times 3[1\bar{1}0]$  presented using the conventional bcc lattice basis. An example of the 72-atoms SQSs is shown in Fig. 1a for a quaternary alloy with equimolar composition. Besides, a SQS with 90 atoms and basis vectors of  $[1\bar{1}\bar{2}] \times 2[111] \times 5[1\bar{1}0]$  was generated to model the ternary alloys with the A<sub>2</sub>B<sub>2</sub>C type of compositions (A, B, and C represent the alloying elements). Moreover, other than the SQSs associated with the compositions listed in Table 1, we also generated an additional

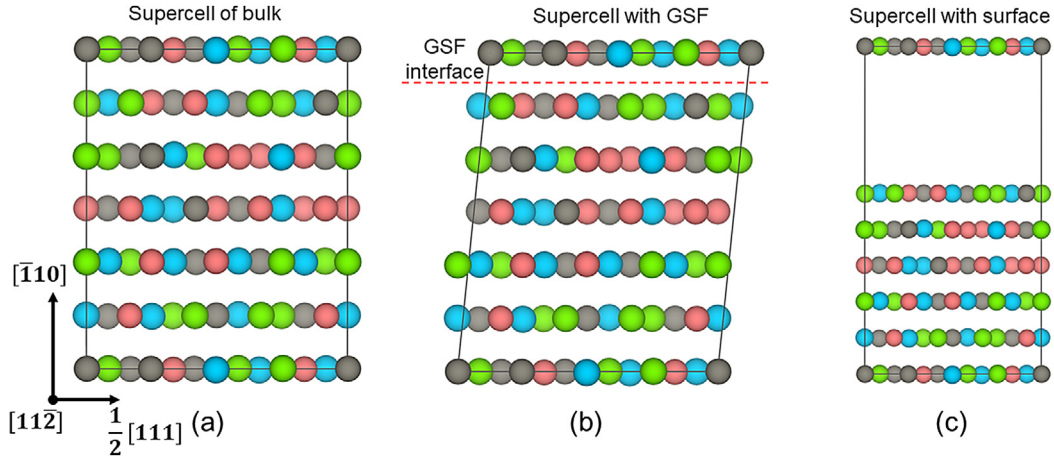


**Fig. 1.** The configurations of (a) the bulk SQS supercell for the quaternary equimolar composition, (b) the supercell for calculations of USF energies, and (c) the supercell for calculations of surface energies. These figures show a projection along the  $[11\bar{2}]$  direction.

**Table 1**  
Alloying systems and compositions studied by the SQS method

Systems	Alloying compositions studied by the SQS method
Binary	Ti <sub>3</sub> Nb, Ti <sub>2</sub> Nb, TiNb, TiNb <sub>2</sub> , TiNb <sub>3</sub> , Ti <sub>3</sub> W, Ti <sub>2</sub> W, TiW, TiW <sub>2</sub> , TiW <sub>3</sub> , TiW <sub>7</sub> , Ti <sub>3</sub> Ru, Ti <sub>2</sub> Ru, TiRu, Hf <sub>3</sub> Nb, Hf <sub>2</sub> Nb, HfNb, HfNb <sub>2</sub> , HfNb <sub>3</sub> , V <sub>7</sub> W, V <sub>3</sub> W, VW, VW <sub>3</sub> , VW <sub>7</sub> , Nb <sub>7</sub> Ta, Nb <sub>3</sub> Ta, NbTa, NbTa <sub>3</sub> , NbTa <sub>7</sub> , Nb <sub>3</sub> Mo, Nb <sub>2</sub> Mo, NbMo, NbMo <sub>2</sub> , NbMo <sub>3</sub> , Nb <sub>3</sub> W, Nb <sub>2</sub> W, NbW, NbW <sub>2</sub> , NbW <sub>3</sub> , Nb <sub>7</sub> Ru, Nb <sub>3</sub> Ru, Nb <sub>2</sub> Ru, NbRu, Ta <sub>7</sub> Mo, Ta <sub>3</sub> Mo, TaMo, TaMo <sub>3</sub> , TaMo <sub>7</sub> , Ta <sub>7</sub> Re, Ta <sub>3</sub> Re, TaRe, TaRe <sub>3</sub> , Mo <sub>7</sub> W, Mo <sub>3</sub> W, MoW, MoW <sub>3</sub> , MoW <sub>7</sub> , W <sub>7</sub> Re, W <sub>3</sub> Re, WRe, WRe <sub>3</sub> , W <sub>7</sub> Ru, W <sub>3</sub> Ru, W <sub>2</sub> Ru
	Ti <sub>2</sub> NbW, Ti <sub>2</sub> Nb <sub>2</sub> W, TiNbW, TiNb <sub>2</sub> W, TiNb <sub>2</sub> W <sub>2</sub> , TiNbW <sub>2</sub> , TiWRe, TiW <sub>2</sub> Re, TiNbRu, TiNb <sub>2</sub> Ru
Ternary	TiZrHfNb, TiZrHf <sub>2</sub> Nb <sub>2</sub> , TiZrHfNb <sub>3</sub> , TiZrVNb, TiZr <sub>2</sub> V <sub>2</sub> Nb, TiVNbMo, TiNbWRe, TiNb <sub>2</sub> WRe, TiNb <sub>2</sub> W <sub>2</sub> Re, TiNbW <sub>3</sub> Re, TiNbWRu, TiNb <sub>2</sub> WRu, TiNb <sub>2</sub> W <sub>2</sub> Ru, TiNbW <sub>3</sub> Ru, VNBWRu, VNB <sub>2</sub> W <sub>2</sub> Ru, VNBW <sub>3</sub> Ru, VMoWRu, VMoW <sub>3</sub> Ru, Nb <sub>2</sub> Ta <sub>2</sub> MoW, NbTaMoW, NbTa <sub>3</sub> MoW, NbTaMoW <sub>3</sub> , Nb <sub>3</sub> TaWRu, Nb <sub>2</sub> TaW <sub>2</sub> Ru, NbMoW <sub>3</sub> Ru, Ta <sub>2</sub> MoW <sub>2</sub> Re, TaMoWRe, TaMoW <sub>3</sub> Re, TaMoWRu, TaMo <sub>2</sub> W <sub>2</sub> Ru, TaMoW <sub>3</sub> Ru

group of 72-atoms quaternary SQSs in order to validate the screening results of the surrogate models Section 3.4.

Both the atomic positions and the geometry (the shape and volume) of the generated SQS supercells are fully relaxed to capture the local lattice distortion induced by the size mismatch between the constituent elements. The results show that the shape changes of these orthogonal supercells are negligible. Then, with the relaxed supercells, a method developed in our previous work [38] is adopted to compute the  $(1\bar{1}0)[111]$  unstable stacking fault energy,  $\gamma_{\text{usf}}$ , and the  $(1\bar{1}0)$  surface energy,  $\gamma_{\text{surf}}$ .

To create a  $(1\bar{1}0)[111]$  generalized stacking fault (GSF) between two neighboring  $(1\bar{1}0)$  planes, the atoms below the fault interface are rigidly shifted relative to the rest of atoms along the  $[111]$  direction. The shift can be accommodated by distorting the bulk supercell (Fig. 1a) to have an angle away from 90 degrees between

the  $[111]$  and  $[1\bar{1}0]$  directions so that only one stacking fault interface is introduced in the supercell, as shown in Fig. 1b. All the atoms in the shifted supercell are relaxed along the  $[1\bar{1}0]$  direction but fixed along the  $[111]$  and  $[11\bar{2}]$  directions. The supercell size is also relaxed along  $[1\bar{1}0]$  direction to remove the normal stress perpendicular to the fault plane. After the relaxation, the GSF energy is calculated as the difference in total energies between the supercells with and without the GSF structure divided by the cross-sectional area parallel to the fault plane.

In the present work, for the sake of simplification, the USF energy ( $\gamma_{\text{usf}}$ ) is treated as the GSF energy at a fixed shift distance that equals to the length of  $\frac{1}{4}[111]$ , although a more rigorous way is to interpolate the maximum point of the GSF energy curve as the function of the shift distance. Our benchmark calculations were performed to show that the difference between the GSF energy at the shift distance of  $\frac{1}{4}[111]$  and the maximum energy from the curve interpolation is actually negligible, which is only as small as around 0.00062 J/m<sup>2</sup>. Details are shown in Section 3.1. In addition, since one supercell contains multiple  $(1\bar{1}0)$  planes, the GSFs between all the possible neighboring planes must be considered. For each of the two neighboring planes, two shifts, namely  $-\frac{1}{4}[111]$  and  $+\frac{1}{4}[111]$ , have been applied to compute the corresponding GSF energies, respectively. Finally, for a given alloy composition, its  $\gamma_{\text{usf}}$  is an average of all the calculated GSF energies by considering all the possible positions of the fault planes in the SQS supercell. For example, for the 72-atom supercell, its  $\gamma_{\text{usf}}$  is calculated by averaging 12 (12 = 6 planes  $\times$  2 directions) individual GSF energies.

To calculate the the surface energy,  $\gamma_{\text{surf}}$ , a vacuum layer of 7 Å is inserted between two neighbouring  $(1\bar{1}0)$  planes to introduce two free surfaces, as shown in Fig. 1c. The total energy of the supercell with free surfaces is computed by only relaxing the atoms on the surface planes and their first-nearest adjacent  $(1\bar{1}0)$  planes. The rest of atoms and the supercell geometry remain fixed. The surface energy is defined as the difference in total energies of the bulk supercell (Fig. 1a) and the supercell with surfaces (Fig. 1c) divided by twice the cross-sectional area parallel to the surface planes. The convergence of the calculated surface energies with respect to the volume of the vacuum region in the supercell was also tested. Similar to  $\gamma_{\text{usf}}$ ,  $\gamma_{\text{surf}}$  of a given alloying composition is also derived by averaging the surface energies of all the  $(1\bar{1}0)$  planes in the SQS supercell. For example,  $\gamma_{\text{surf}}$  of the 72-atoms supercell is calculated by averaging over six individual  $(1\bar{1}0)$  planes.

Additionally, it is worth mentioning that the convergence of the calculations on  $\gamma_{\text{usf}}$  and  $\gamma_{\text{surf}}$  was also tested using a series of SQSs with different sizes, as discussed in detail in Section 3.1. With the

**Table 2**

The electronic configurations of the pseudopotentials used in the first-principles calculations. The electrons in the bracket are treated as inner-core electrons.

Element	Ti_sv	Zr_sv	Hf_pv
V_RHFIN	([Ar])3s <sup>2</sup> 3p <sup>6</sup> 3d <sup>2</sup> 4s <sup>2</sup>	([Kr])4s <sup>2</sup> 4p <sup>6</sup> 4d <sup>2</sup> 5s <sup>2</sup>	([Xe])4f <sup>14</sup> 5p <sup>6</sup> 5d <sup>2</sup> 6s <sup>2</sup>
Element	V_sv	Nb_sv	Ta_pv
V_RHFIN	([Ar])3s <sup>2</sup> 3p <sup>6</sup> 3d <sup>3</sup> 4s <sup>2</sup>	([Kr])4s <sup>2</sup> 4p <sup>6</sup> 4d <sup>3</sup> 5s <sup>2</sup>	([Xe])4f <sup>14</sup> 5p <sup>6</sup> 5d <sup>3</sup> 6s <sup>2</sup>
Element	Mo_pv	W_pv	Re
V_RHFIN	([Kr])4p <sup>6</sup> 4d <sup>4</sup> 5s <sup>2</sup>	([Xe])4f <sup>14</sup> 5p <sup>6</sup> 5d <sup>4</sup> 6s <sup>2</sup>	([Xe])4f <sup>14</sup> 5d <sup>5</sup> 6s <sup>2</sup>
Element	Ru		
V_RHFIN	([Kr])4d <sup>6</sup> 5s <sup>2</sup>		

calculated  $\gamma_{\text{usf}}$  and  $\gamma_{\text{surf}}$ , the D parameter, which qualitatively reflects the potency of the intrinsic ductility of a material [31–34,61], can be easily derived as,

$$D = \gamma_{\text{surf}}/\gamma_{\text{usf}} \quad (1)$$

### 2.1.2. Parameter settings of DFT calculations

In the present work, the DFT calculations were carried out using the Vienna ab-initio simulation package (VASP) [62]. The projector augmented wave method (PAW) [63] and the exchange-correlation functional depicted by the general gradient approximation from Perdew, Burke, and Ernzerhof (GGA-PBE) [64] were employed to perform the calculations. The electronic configurations of the pseudopotentials used for the first-principles calculations are summarized in Table 2. The energy cutoff of the plane-wave basis was set to be 400 eV. A first-order Methfessel Paxton smearing of 0.2 eV was applied for Brillouin zone integration. To accommodate the differences in the size of the supercell structures, the automatic meshing scheme, as implemented in the VASP software, was used to generate the k-point grids in the first Brillouin zone of the calculations. The  $R_k$  length of the automatic meshing was set to be 30 Å. The resulting k-point grids are  $4 \times 2 \times 3$  for the 72-atom supercell in both the undeformed bulk and GSF configurations,  $4 \times 1 \times 3$  for the 72-atom supercell in the surface configurations, and  $4 \times 1 \times 3$  for the 90-atom supercells in either bulk or defect configurations. The here employed k-point density and smearing width were determined based on a set of convergence test calculations to accommodate a balance between calculation accuracy and efficiency. The relative deviations of the current results from those calculated using a much denser k-point mesh are about 4 to 5 times smaller than the deviations caused by multiple (110) planes in an SQS cell. The energy convergence criterion of the electronic self-consistency cycle is  $10^{-6}$  eV for all the calculations. For the calculations of USF and surface energies, the relaxation process is terminated when the force on each atom is less than 20 meV/Å.

## 2.2. Surrogate models based on statistical regression

Developing surrogate models for reliable predictions of USF and surface energies is necessary and crucial to enable a systematic screening of those alloy properties in a vast compositional space. In this subsection, we first describe how the descriptors for the surrogate model can be derived based on a method developed in the present work. Second, we introduce the details of a statistical regression framework used in the present work to construct the surrogate models. This framework was developed previously and has been successfully applied for modeling elastic stiffness of ordered inorganic compounds [65].

### 2.2.1. Physics-informed descriptors

Generating GSF and surface defects in crystals are intrinsically associated with the stretching, breaking and reforming of atomic bonds. Drawing on the idea of the bond-counting model [66,67],

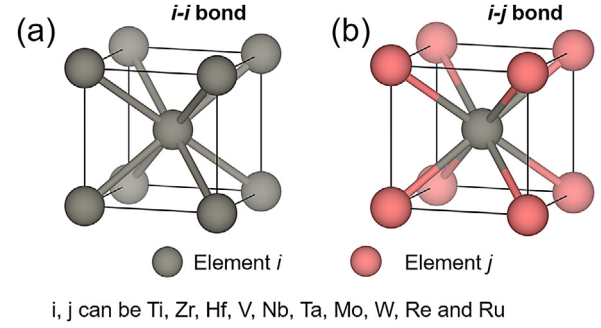


**Fig. 2.** Schematic illustration of the first-nearest neighbor bonds in (a) the single-element bcc and (b) binary B2 structures.

we developed a method to effectively construct a set of descriptors, which include both the information of alloy compositions and interatomic bonding characteristics.

In an ideally mixed solid-solution alloy, atoms are not orderly organized but randomly distributed on lattice sites. The probability for two constituent elements,  $i$  and  $j$ , to form the  $i$ - $j$  type of atomic bonds should equal to the product between the chemical compositions of the two elements. Based on the concept of the bond-counting model [66,67], we can approximate a certain physical property of an alloy, such as the cohesive energy, as a summation of the individual contributions from each atomic bond. Therefore, for the random alloys, this summation can be considered as a weighted average of the values of a physical feature, such as bond energy, associated with each type of atomic bonds. Correspondingly, the weighting factor is the presence probability of each type of atomic bonds in the alloy, which can be calculated from the alloy compositions as described above. Therefore, following the same logic, the descriptors for the surrogate models were derived as,

$$u_p = \sum_i x_i \sum_j x_j p_{ij} \quad (2)$$

Here  $x_i$  and  $x_j$  are the chemical compositions (measured in the mole fractions) of element  $i$  and  $j$ , respectively, which are among the 10 refractory elements studied in the present work (i.e., Ti, Zr, Hf, V, Nb, Ta, Mo, W, Re and Ru).  $u_p$  is a descriptor developed from a bond feature parameter  $p$ , which has a value of  $p_{ij}$  for the  $i$ - $j$  type of atomic bonds. Apparently,  $p_{ij}$  can be written as a  $10 \times 10$  matrix, in which each component corresponds to a pair permutation between the 10 alloying elements. In addition, to reflect the fluctuations in local atomic environments, the weighted standard deviation of  $u_p$  is also considered as a descriptor ( $u_p^\sigma$ ), which is expressed as,

$$u_p^\sigma = \sqrt{\left(\frac{1}{1 - \sum_i x_i^2}\right) \cdot \left(\sum_i x_i \left(\sum_j x_j p_{ij} - u_p\right)^2\right)} \quad (3)$$

As a simplification, we only consider the atomic bonds in the first-nearest neighbor (FNN) shell during the bond counting process. Consequently, we could apply the physical and electronic properties of the single-element bcc and ordered binary B2 structures as the bond feature parameters,  $p_{ij}$ , in Eq. 2. This is because, in a single-element bcc structure (e.g., composed of element  $i$ ), the only type of the FNN atomic bond is the  $i$ - $i$  bond along the {111} direction as shown in Fig. 2a. Similarly, in a B2 structure composed of element  $i$  and  $j$ , the only type of the FNN bond is the  $i$ - $j$  bond shown in Fig. 2b. As an example, if we consider the cohesive energy ( $E_c$ ) as a bond feature parameter, its  $p_{ii}$  component thus equals to  $E_c$  of the single-element bcc structure for the  $i$ - $i$  bond, while  $p_{ij}$  and  $p_{ji}$  both equal to  $E_c$  of the binary B2 structure for the  $i$ - $j$  and  $j$ - $i$  bond, respectively.



Since the single-element bcc and B2 structures are both ordered and highly symmetric, DFT calculations can be applied to generate a group of  $p_{ij}$  without huge computational costs. Specifically, we performed DFT calculations to model all the possible single-element bcc and binary B2 structures constituted by the alloying elements studied in the present work. Their associated USF and surface structures were also modeled. All bond feature parameters were obtained from the calculations of the fully relaxed bcc and binary B2 structures with their equilibrium lattice constants if possible. However, among all the modeled bcc and B2 structures (55 individual structures in total), we found that there are 13 structures are mechanically unstable in response to shear deformations as their elastic constants do not satisfy one of the "Born stability criteria" [68], where  $c_{11} - c_{12}$  should be positive. The mechanically unstable structures include the bcc and B2 structures only composed of the group IV elements, bcc Re, bcc Ru, and the B2 structures of NbRu, TaRu, MoRu, WRu, and ReRu. Correspondingly, for those mechanically unstable structures, DFT relaxations were performed by specifically constraining the simulation cell to remain cubic symmetry. The subsequent calculations on the bond feature parameters ( $p_{ij}$ ) for descriptor construction were based on these relaxed symmetry-constrained B2 structures.

From the DFT calculations, several physical properties of the pure elements and ordered B2 intermetallics were derived and employed as bond feature parameters,  $p_{ij}$ , respectively, including the USF energy ( $\gamma_{\text{usf}}^{\text{bcc/b2}}$ ), surface energy ( $\gamma_{\text{surf}}^{\text{bcc/b2}}$ ), cohesive energy ( $E_c^{\text{bcc/b2}}$ ) and equilibrium atomic volume ( $V_{\text{eq}}^{\text{bcc/b2}}$ ).  $E_c^{\text{bcc/b2}}$  and  $V_{\text{eq}}^{\text{bcc/b2}}$  were calculated by using the perfect bulk structures.  $\gamma_{\text{usf}}^{\text{bcc/b2}}$  and  $\gamma_{\text{surf}}^{\text{bcc/b2}}$  were calculated by using the same supercell method as described in Section 2.1.1. The supercell used for the GSF and surface energy calculations for the pure metals originally has a geometry of  $[11\bar{2}] \times 1/2[111] \times 3[1\bar{1}0]$  before adding the shear or the vacuum layer, while the geometry of the supercell used for the calculations of the ordered B2 intermetallics is  $[11\bar{2}] \times [111] \times 3[1\bar{1}0]$ . These supercells have the same basis vectors as the 72-atom SQS supercells along the  $[11\bar{2}]$  and  $[1\bar{1}0]$  directions but shorter lengths along the  $[111]$  direction due to the higher symmetries of the bcc and ordered B2 structures. The calculations of the bulk references of the bcc and binary B2 structures were performed with the conventional 2-atom cubic cells.

Additionally, our previous work has shown that the solute-defect interactions in refractory metals are quantitatively correlated with a group of electronic parameters [39,43]. These parameters can quantitatively describe the variations in the local electronic density of states (LDOS) of the atoms near a defect relative to those of the atoms in perfect bulk lattices. Therefore, a part of those electronic parameters were also used for the descriptor constructions. These parameters include the first and second order moments of the valance  $d$ - and  $sp$ -orbital LDOSs and the bimodality of the valance  $d$ -orbital LDOSs [43]. The LDOSs are the projected DOSs of the atoms in the bulk lattice, on the surfaces, or on stacking fault planes of the single-element bcc metals and binary B2 alloys. The first-order moment of a LDOS ( $\epsilon_k^1$ ) is defined as,

$$\epsilon_k^1 = \frac{\int_{-\infty}^{+\infty} E \rho_k(E) dE}{\int_{-\infty}^{+\infty} \rho_k(E) dE} \quad (4)$$

where  $\rho_k(E)$  is the DFT-calculated LDOS of the orbital  $k$ , and  $k$  can be either the valance  $d$ - or  $sp$ - orbitals in the present work.  $E$  is the band energy. Then, based on  $\epsilon_k^1$ , the second moment ( $\epsilon_k^2$ ) is calculated as,

$$\epsilon_k^2 = \frac{\int_{-\infty}^{+\infty} (E - \epsilon_k^1)^2 \rho_k(E) dE}{\int_{-\infty}^{+\infty} \rho_k(E) dE} \quad (5)$$

It should also be noted that the axis of the band energy was scaled to set the Fermi energy as zero for the integrations of Eq. 4 and 5. Moreover, as shown in Table 2, the pseudopotentials of some elements include the semi-core  $s$  or  $p$  electrons as valence electrons for the first-principles calculations. However, it is found that the LDOSs of these semi-core electrons are localized at very low energy states and have a very large energy gap with the outermost  $s$ ,  $p$  and  $d$  orbitals. We thus assume these semi-core electrons having very limited contributions to electronic bonding. Therefore, the LDOSs of these semi-core electrons are not included in the band analysis based on Eq. 2 and 3. Additionally, the bimodality of a LDOS can be measured through the Hartigan's dip test, which was described in detail in Ref [43].

Furthermore, for the mechanically unstable bcc and B2 structures, the symmetry-constrained calculations cannot accurately predict their free energy as well as other physical properties at the ground state. Nevertheless, the results of those symmetry-constrained calculations are still useful for the purpose of constructing descriptors. We hypothesize that the energetic, structural and electronic properties of these bcc and B2 structures could effectively represent the bonding features (e.g., stability to shear deformations) between the same types of first-nearest neighbors in the alloys with a bcc lattice. For example, the USF energies of the mechanically unstable B2 structures were calculated to be negative relative to the symmetry-constrained bulk reference, indicating the atomic bonds in the B2 structure are unstable to the shear deformation. When the same type of atomic bonds appears in the lattice of a bcc solid-solution alloy, they are likely to also be unstable to yield negative contributions to the USF energy of the alloy. These negative contributions can be captured by including the negative USF energies of the symmetry-constrained B2 structure as one of the bond feature parameters to construct descriptors. On the other hand, it should be noted that the ground-state properties of the chemical compositions of these mechanically unstable phases can be appropriately predicted by implementing computational methodologies without the symmetry constrain, such as the method considering the hopping of the system between different local minima near the ideal high-symmetry structure [69–71]. These methodologies could be a better solution in the future to construct the descriptors for the material properties beyond a fixed lattice.

Moreover, two features of elemental properties, the numbers of valance electrons and the Pauling electronegativity, are also used to construct the descriptors in the present work. Specifically, the descriptors were calculated as,

$$u_q = \sum_i x_i q_i \quad (6)$$

$$u_q^\sigma = \sqrt{\left(\frac{1}{1 - \sum_i x_i^2}\right) \cdot \left(\sum_i x_i (q_i - u_q)^2\right)} \quad (7)$$

Here  $q_i$  represents either the numbers of valance electrons or the Pauling electronegativity of element  $i$ , and  $x_i$  represents the chemical composition of element  $i$ . The descriptors generated by Eq. 6 and 7 are intended to describe the average filling level of the  $d$ -bands and the tendency of charge transfer between different elements, respectively.

Table A1 lists all the atomic bond parameters ( $p_{ij}$ ) and elemental properties ( $q_i$ ) used for descriptors construction in the present work. Each of them results in two descriptors: one relates to the arithmetic mean Eq. 2 and (6) and the other one relates to the weighted standard deviation of the mean Eq. 3 and (7). Therefore, 42 descriptors were generated in total. Only 30 of 42 descriptors were employed as input variables for the regression of  $\gamma_{\text{usf}}$ , where the descriptors associated with the surface structures were

not used. In the same way, when the regression was performed for  $\gamma_{\text{surf}}$ , the descriptors associated with the stacking faults were not used.

### 2.2.2. Statistical regression framework

In the present work, a statistical regression framework [65], namely Gradient Boosting Machine Local Polynomial Regression (GBM-Locfit), was used to perform the regression analysis and obtain quantitative models to predict  $\gamma_{\text{usf}}$  and  $\gamma_{\text{surf}}$  of bcc solid-solution alloys. In the GBM-Locfit framework, the gradient boosting machine iteratively produces a prediction model in the form of an ensemble of predictive functions,  $\eta_i$ . At each GBM-iterative step  $i$ ,  $\eta_i$  is generated from a regression model implemented in the Locfit package [72], which performs kernel-based multivariate locally linear regressions. Only a subset of the input descriptors was used to perform the locally linear regression and generate  $\eta_i$ . This subset of descriptors was obtained by performing many individual locally linear regressions by traversally using all the possible subsets of the input descriptors and subsequently picking the subset that leads to the lowest regression error. For the regression of  $\gamma_{\text{usf}}$ , the size of the subset is set to not exceed three descriptors, while this limit is set to be 2 for the regression of  $\gamma_{\text{surf}}$ . As a result, only a portion of the input descriptors was eventually selected and used by the GBM-Locfit framework [65], which could reduce the risk of over-fitting. The final prediction model was derived as the sum of all the predictive functions, while each function was attenuated by a learning rate of 0.1. Moreover, the GBM-locfit framework is performed with  $n$ -fold cross-validation ( $n$  depends on the numbers of regression samples) and a conservative risk criterion to determine an optimal number of iteration steps [65,73], which could also lower the risk of over-fitting.

Due to the high computational cost, the DFT calculations with the SQS method were only able to generate the  $\gamma_{\text{usf}}$  and  $\gamma_{\text{surf}}$  data for a finite amount of bcc solid-solution alloys (Table 1). Therefore, the obtained DFT data were not randomly split into two partitions for training and testing. Instead, we specifically trained the surrogate models with the data of binary and ternary alloys only, and used the rest quaternary data as the test set. This training and testing scenario allows us to maximally validate the prediction capability of the surrogate models for multicomponent alloy compositions. The validation results are discussed in Section 3.3 in detail. After the validation, the surrogate models were updated by re-training with all the data listed in Table 1 for screening purposes.

The screening predictions from the newly updated models were further validated by an additional set of DFT calculations as described in Section 3.4 and Table 3.

## 3. Results and Discussions

### 3.1. Verification of the computational approach for $\gamma_{\text{usf}}$ and $\gamma_{\text{surf}}$

By definition, the unstable stacking fault energy,  $\gamma_{\text{usf}}$ , corresponds to the maximum value of the GSF curve along the slip direction.  $\gamma_{\text{usf}}$  is generally obtained by interpolating the results of a series of GSF calculations performed at different shift distances. This will severely increase the computational cost if the target is to investigate  $\gamma_{\text{usf}}$  for a large amount of alloying compositions, for example, 106 compositions in the present work. On the other hand, due to the mirror symmetry of the  $(1\bar{1}0)$  plane,  $\gamma_{\text{usf}}$  of the  $(1\bar{1}0)[111]$  slip in a bcc lattice should occur at a shift distance of  $|\frac{1}{4}[111]|$  although deviations may be induced by the local chemical variations and lattice distortions [42]. In the present work, for the sake of simplification, we used the GSF energies that correspond to the  $|\frac{1}{4}[111]|$  shifts on different fault planes in the supercell to derive the averaged  $\gamma_{\text{usf}}$  for a given alloy composition. Therefore, benchmark calculations are necessary to verify such simplification.

Here, using the equimolar TiW alloy as an example, benchmark calculations were performed to investigate the difference between the GSF energy at a shift of  $|\frac{1}{4}[111]|$  (referred as the geometric  $\gamma_{\text{usf}}$  in the following) and the maximum value interpolated from the GSF curve (referred as the interpolated  $\gamma_{\text{usf}}$  in the following). As shown in Fig. 3a, the relaxed supercell structure of the TiW alloy has six individual interfaces between the neighboring  $(1\bar{1}0)$  planes to generate stacking faults. Each of these interfaces should have two sets of GSF energies corresponding to the shifts along the  $-\vec{b}$  and  $\vec{b}$  directions, respectively, where  $\vec{b}$  is the Burgers vector  $\frac{1}{2}[111]$ . For a given shift direction of a specific interface, we first calculated the GSF energies at a shift of  $0.5|\vec{b}|$ , which yield the values of the geometric  $\gamma_{\text{usf}}$ . Then, additional calculations were performed at shifts of  $0.375|\vec{b}|$ ,  $0.4375|\vec{b}|$ ,  $0.5625|\vec{b}|$ , and  $0.625|\vec{b}|$ , respectively. Together with the GSF energies at  $0.5|\vec{b}|$ , a second-order polynomial fitting was performed for the five data points with respect to their shift distances. The maximum of the fitted polynomial yields the value of the interpolated  $\gamma_{\text{usf}}$ . The  $R^2$  of the fittings for all the interfaces were found to be close to 1 ( $>0.99$ ),

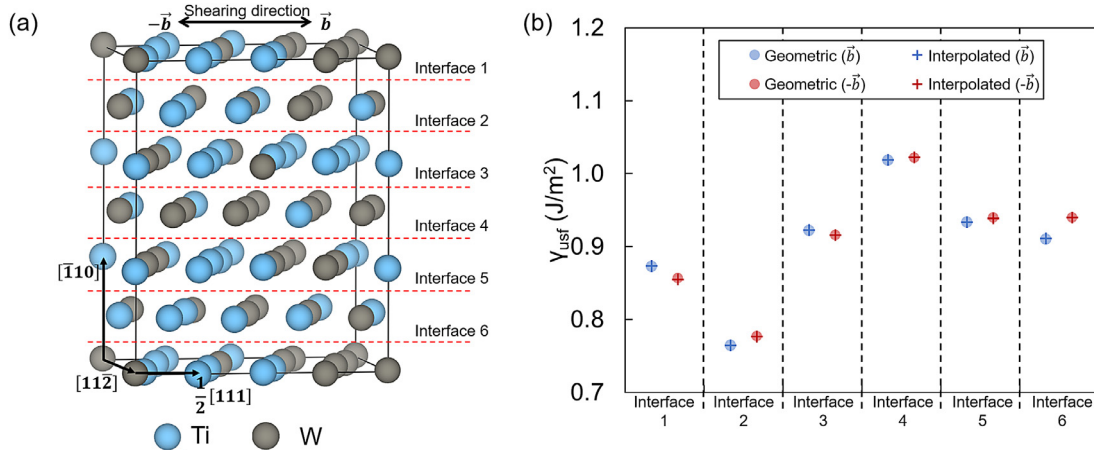


**Fig. 3.** (a) The supercell structure for the equimolar TiW alloy after relaxation. To obtain the final averaged  $\gamma_{\text{usf}}$  of the supercell, calculations of GSF energies have to be performed for six individual interfaces, and each interface has two shift directions ( $-\vec{b}$  and  $\vec{b}$ ). (b) The geometric  $\gamma_{\text{usf}}$  (circle symbols) of different interfaces marked in Fig. 3a in comparison with the corresponding interpolated  $\gamma_{\text{usf}}$  (cross symbols). The data points corresponding to the shift along the  $\vec{b}$  direction are marked in blue color, while those associated with the opposite shift direction are marked in red color. The geometric  $\gamma_{\text{usf}}$  corresponds to the GSF energy at a shift of  $|\frac{1}{4}[111]|$ . The interpolated  $\gamma_{\text{usf}}$  is derived by interpolating the maximum point of the GSF curve.

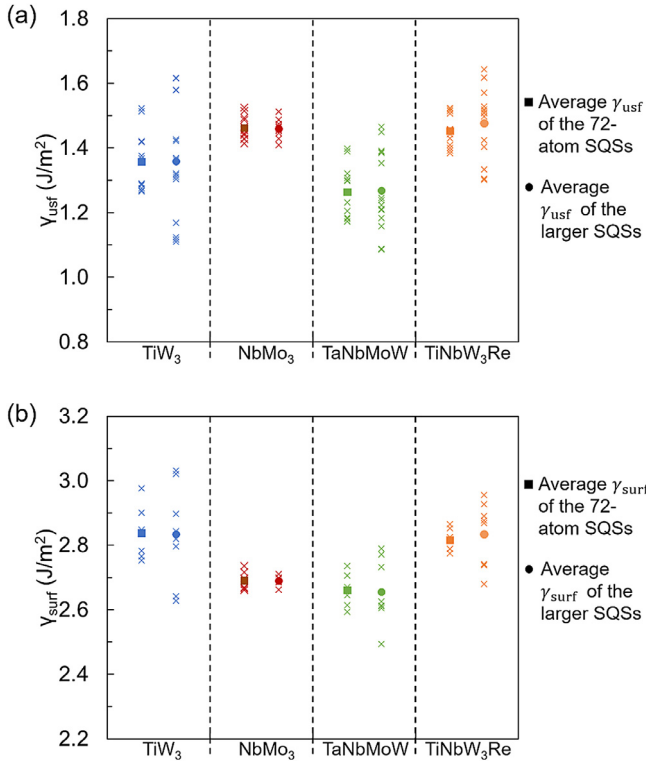


**Fig. 4.** (a) Unstable stacking fault energies and (b) surface energies of the TiW<sub>3</sub>, NbMo<sub>3</sub>, TaNbWMo and TiNbW<sub>3</sub>Re alloys calculated using the SQS supercells with different sizes. For each of the alloy compositions, the solid cubic or circle symbol corresponds to the averaged  $\gamma_{\text{usf}}$  and  $\gamma_{\text{surf}}$  calculated using the original 72-atoms supercell or a larger supercell, respectively. The cross symbols correspond to the individual values of  $\gamma_{\text{usf}}$  and  $\gamma_{\text{surf}}$  due to the different choices on the positions of the defect planes in the supercell.

which means that the GSF curve around its maximum can be well described by a second-order polynomial. Fig. 3b shows a comparison between the values of the geometric and interpolated  $\gamma_{\text{usf}}$  for each of the possible interfaces and shift directions in the supercell of Fig. 3a. The energy difference between the geometric and interpolated  $\gamma_{\text{usf}}$  is only about 0.00062 J/m<sup>2</sup> with a standard deviation of 0.00036 J/m<sup>2</sup> by averaging over different fault planes. This energy difference is almost negligible compared to the difference in the GSF energies of different fault interfaces. Since the final  $\gamma_{\text{usf}}$  of the supercell is derived by averaging the results over all the interfaces along both shift directions, using the GSF energy at a shift of  $|\frac{1}{4}[111]|$  for the derivation will not notably impact the accuracy of results. Meanwhile, the computational efficiency is significantly improved.

Furthermore, benchmark calculations were also performed to evaluate the convergence of the calculated  $\gamma_{\text{usf}}$  and  $\gamma_{\text{surf}}$  with respect to the size of the SQS supercells. Using the ATAT code [37], four individual SQS supercells with sizes larger than the original 72-atom supercell were additionally generated for the alloy compositions of TiW<sub>3</sub>, NbMo<sub>3</sub>, TaNbWMo and TiNbW<sub>3</sub>Re, respectively. Specifically, the basis vectors of these additionally generated SQS supercells are  $[11\bar{2}] \times 2[111] \times 4[1\bar{1}0]$ ,  $2[11\bar{2}] \times 2[111] \times 3[1\bar{1}0]$ ,  $[11\bar{2}] \times 2[111] \times 4[1\bar{1}0]$ , and  $[11\bar{2}] \times 3[111] \times 4[1\bar{1}0]$ , respectively. As a comparison, the basis vectors of the original 72-atom supercell are  $[11\bar{2}] \times 2[111] \times 3[1\bar{1}0]$ . Then, following the same method described in Section 2.1.1, we calculated  $\gamma_{\text{usf}}$  and  $\gamma_{\text{surf}}$  using these larger supercells, and compare the results with those using the original 72-atom supercell. As shown in Fig. 4, increasing the supercell size has very limited effects on the averaged  $\gamma_{\text{usf}}$  and  $\gamma_{\text{surf}}$ , even though it could result in larger deviations among the in-

dividual USF and surface energies that correspond to the different choices on the positions of the defect planes in the supercell.

### 3.2. DFT results on $\gamma_{\text{usf}}$ and $\gamma_{\text{surf}}$

The results of DFT calculations on  $\gamma_{\text{usf}}$ ,  $\gamma_{\text{surf}}$  and the  $\frac{\gamma_{\text{surf}}}{\gamma_{\text{usf}}}$  ratio (i.e. the  $D$  parameter defined in Eq. 1) of the alloy compositions listed Table 1 are summarized in Table B1 in Appendix B. In the following, we further discuss the correlations of these results with the filling fraction of the valence  $d$  orbitals as shown in Fig. 5. Previous work has shown that the  $d$ -band filling effect is generally essential in determining physical and mechanical properties of the transition metal elements and their alloys [28,43,74,75].

$\gamma_{\text{usf}}$  and  $\gamma_{\text{surf}}$  of various binary alloys are plotted with respect to the alloy's valence electron concentration (VEC) in Fig. 5a and 5b, respectively. The VEC of an alloy is calculated as the average over the number of valence electrons of the constituent elements with respect to their mole fractions (unit:  $e^-/\text{atom}$ ). In transition metal alloys, a higher value of VEC corresponds to a higher average filling fraction of the valence  $d$ -bands. In the present work, the valence electrons of an element are considered as its outermost  $s$  and  $d$  electrons. Specifically, for the 3d elements, only the 3d and 4s electrons are considered as valence electrons. The same definition of valence electrons are used for the 4d and 5d elements. The binary alloys in Fig. 5a and 5b are selected from nine different alloy systems as they are representative to show clear trends of the USF and surface energies with respect to VEC. Clearly, both  $\gamma_{\text{usf}}$  and  $\gamma_{\text{surf}}$  of the binary alloys show a nearly parabolic dependence on the variations of VEC. In a range of VEC from 4.0 to 6.5  $e^-/\text{atom}$ ,  $\gamma_{\text{usf}}$  and  $\gamma_{\text{surf}}$  first increase with VEC to reach a maximum, and then decrease with the further increases of VEC. It is interesting to note that the highest  $\gamma_{\text{usf}}$  does not correspond to pure bcc W but the VW<sub>7</sub> alloy with a VEC of 5.875  $e^-/\text{atom}$ . This indicates that the mechanical strength of the group VI metals can be further enhanced by properly alloying them with a small amount of group IV or V metals. However, over alloying of group IV or V metals could produce a softening effect due to the parabolic behavior of  $\gamma_{\text{usf}}$ . Similar results were also reported for the ideal tensile behavior of binary refractory alloys [28,29].

Moreover, it is noted that the quantitative dependences of  $\gamma_{\text{usf}}$  and  $\gamma_{\text{surf}}$  on VEC are very different between individual binary systems. In other words, for different alloy compositions with the same VEC, their  $\gamma_{\text{usf}}$  and  $\gamma_{\text{surf}}$  can still vary significantly. For example, as shown in Fig. 5a,  $\gamma_{\text{usf}}$  of the NbMo<sub>3</sub> alloy is calculated to be about 50% higher than that of the Nb<sub>3</sub>Ru alloy, even though both two alloys have the VEC of 5.75  $e^-/\text{atom}$  and are composed of the elements in the same period. The large differences in USF and surface energies are also observed among the binary alloys with identical VECs in the Ti-W, Ti-Nb, V-W and Nb-W systems. Additionally, as shown in Fig. 5c, the  $D$  parameter of the binary alloys also qualitatively shows an approximately parabolic function of VEC, but in an inverse manner to that of  $\gamma_{\text{surf}}$  and  $\gamma_{\text{usf}}$ . Expect for the Nb-Ru system, the curves of other alloy systems are almost overlapped in the range of VEC from 5.25 to 6.25  $e^-/\text{atom}$ , where the alloys also generally have a large  $\gamma_{\text{usf}}$ . The results suggest that a binary refractory alloy that corresponds to a higher mechanical strength would generally have a poorer ductility, vice versa. Therefore, it is difficult to simultaneously improve both the mechanical strength and ductility of binary refractory alloys by tuning their chemical compositions.

Interestingly, it is found that the correlations of the USF and surface energies with VEC in multicomponent refractory alloys is ambiguous and much weaker compared to that of the binary alloys. As shown in Fig. 5d and 5e,  $\gamma_{\text{usf}}$  and  $\gamma_{\text{surf}}$  of the ternary and quaternary alloys listed in Table 1 are also plotted against their VEC values, respectively. Clearly, there are multiple alloys that have

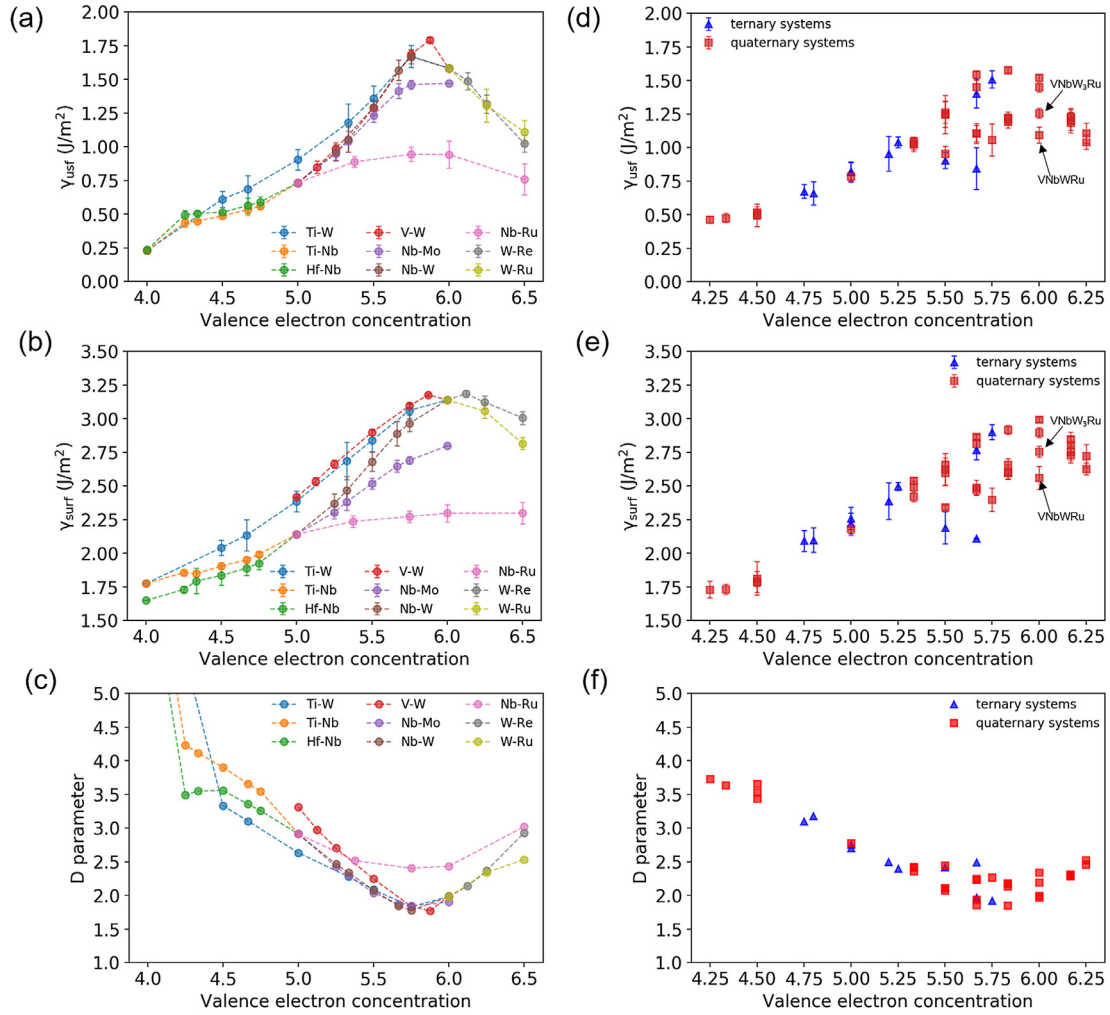


**Fig. 5.** The unstable stacking fault energy ( $\gamma_{\text{usf}}$ ), surface energy ( $\gamma_{\text{surf}}$ ) and  $D$  parameter of the bcc refractory alloys plotted with respect to the valence electron concentration (VEC) of the alloys (unit:  $e^-/\text{atom}$ ). The alloys from the same binary system are marked by the same color. Each of the binary systems corresponds to an individual color in the legend. (d)  $\gamma_{\text{usf}}$ , (e)  $\gamma_{\text{surf}}$ , and (f)  $D$  parameter of the ternary (blue triangles) and quaternary alloys (red squares) plotted with respect to the VEC of the alloys. It should be noted that each of the data points in (a), (b), (d) and (e) corresponds to an average value of  $\gamma_{\text{usf}}$  or  $\gamma_{\text{surf}}$  for an alloy composition, which is obtained by taking an average over all the possible locations of the defect planes in the SQS supercell. The error bar corresponds to the standard deviation of the average.

the same VEC but very different USF and surface energies compared with each other. Even for the alloys with the same constituent elements, their  $\gamma_{\text{usf}}$  and  $\gamma_{\text{surf}}$  are still not solely determined by VEC, such as the VNbWRu and VNbW<sub>3</sub>Ru alloys marked by arrows in Fig. 5d and 5e. These results suggest that simply comparing the VEC values between two multicomponent alloys may not be able to even qualitatively distinguish the difference in their USF and surface energies. As shown in Fig. 5f, the  $D$  parameter of the multicomponent alloys are also distributed in a more scattered pattern on VEC compared to that of the binary alloys. These results are expected because the original  $d$ -band filling effects on alloy properties, such as cohesive energies, were derived using the classical Friedel model [1] by assuming the DOS of  $d$  orbitals has a fixed rectangular shape, which is not accurate in realistic alloys [43].

### 3.3. Predictive ability of the surrogate model

Although the DFT calculations with the SQS method provide means to predict the USF and surface energies for the ideally mixed solid-solution alloys, it is still practically infeasible to directly apply it for screening a vast compositional space due

to the extensive computational cost. Therefore, as described in Section 2.2, surrogate models were developed for more efficient predictions on the USF and surface energies.

To evaluate the prediction capability of the surrogate models, especially for multicomponent alloy systems, we specifically trained the model only with the DFT data of the binary and ternary alloys listed in Table 1 (74 individual alloy compositions in total), and employed the rest quaternary data (32 individual alloy compositions in total) as a test set never used for training. The training and testing results of the surrogate model on  $\gamma_{\text{usf}}$  are presented in Fig. 6a, where the model predictions are plotted against the results of DFT calculations. As shown by the grey dots in Fig. 6a,  $\gamma_{\text{usf}}$  of the alloys in the training set are well reproduced by the surrogate model, yielding a root-mean-squared error (RMSE) of 0.047 J/m<sup>2</sup> and a  $R^2$  value about 0.984. Moreover, as shown by the red dots in Fig. 6a, by only trained with the binary and ternary data, the model can provide reliable predictions for the quaternary alloys in the test set. The RMSE of the model predictions on the test set is only about 0.043 J/m<sup>2</sup>, close to that of the training set, and the corresponding  $R^2$  value for testing is 0.980.

In the same way, the training and testing performance of the surrogate model on  $\gamma_{\text{surf}}$  is illustrated in Fig. 6b. It also is shown



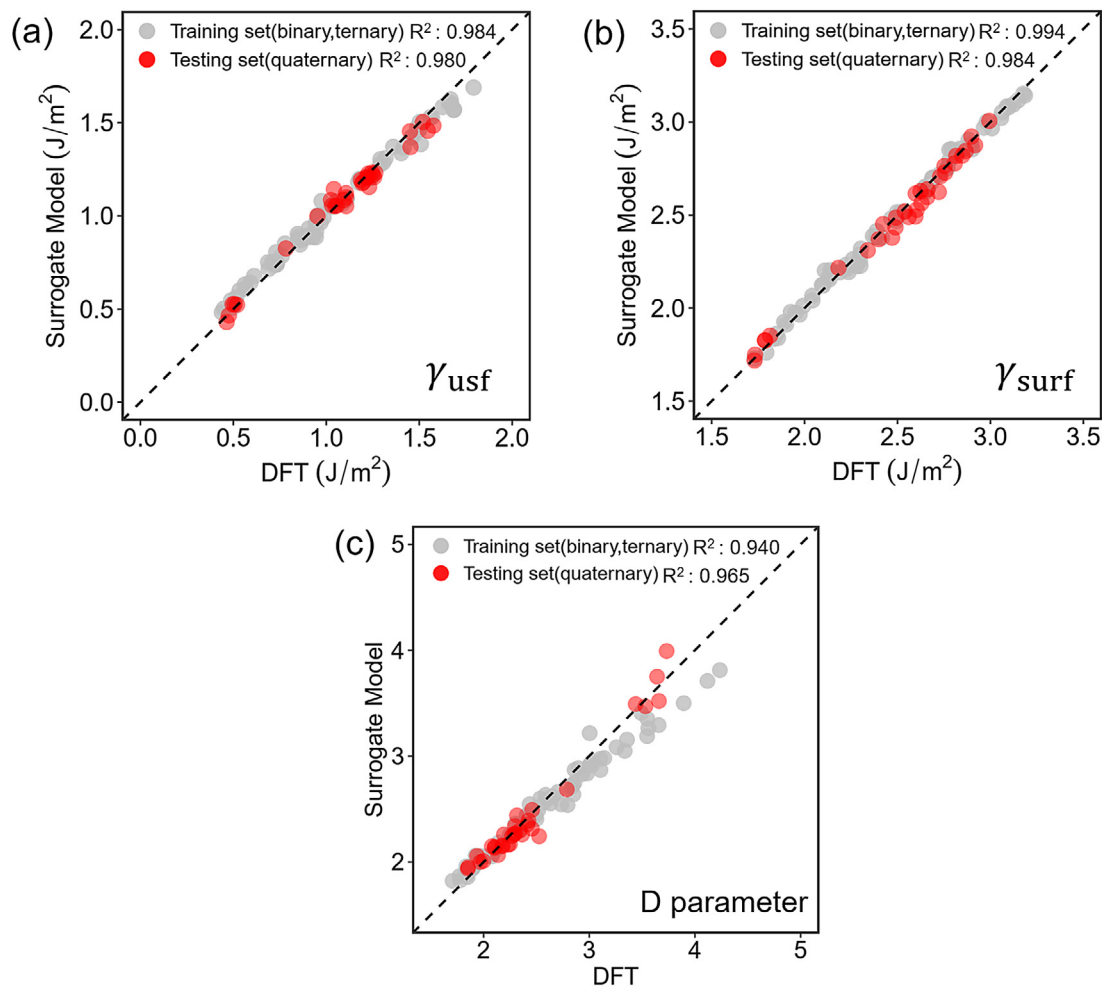


**Fig. 6.** Training and testing performance of the developed surrogate models for (a) unstable stacking fault energy ( $\gamma_{\text{usf}}$ ), (b) surface energy ( $\gamma_{\text{surf}}$ ), and (c)  $D$  parameter. The training set is only composed of the binary and ternary alloys in Table 1. The test set is composed of the quaternary alloys in Table 1. The data of the training and test set are marked in gray and red color, respectively. Additionally, it should be noted that the  $D$  parameter was never used as a regression response to train the surrogate model. The predictions of the surrogate model in (c) are derived from the corresponding predictions on  $\gamma_{\text{usf}}$  and  $\gamma_{\text{surf}}$  based on Eq. 1.

that the model trained only based on the binary and ternary data is able to accurately predict  $\gamma_{\text{surf}}$  of the quaternary alloys in the test set. The RMSE of the predictions on  $\gamma_{\text{surf}}$  is 0.030 and 0.046 J/m<sup>2</sup> for the training and test set, respectively, while the corresponding  $R^2$  value is 0.994 and 0.984, respectively. Furthermore, it is worth noting that none of the alloys in the training set includes Zr as their constituent elements but the models still accurately predict  $\gamma_{\text{usf}}$  and  $\gamma_{\text{surf}}$  for the Zr-containing alloys in the test set. The results of Fig. 6a and 6b support that the developed surrogate models can efficiently and effectively predict the variations of the USF and surface energies in a large compositional space for the bcc refractory alloys.

Additionally, with the predictions of the surrogate models on  $\gamma_{\text{usf}}$  and  $\gamma_{\text{surf}}$ , the  $D$  parameter of the alloys in both training and test sets can be easily derived based on Eq. 1. As shown in Fig. 6c, the values of the  $D$  parameter derived from the model predictions are generally in good agreement with the results obtained from the DFT calculations. In addition, for the alloys in the training set with relatively larger  $D$  parameters, the results from the surrogate models seem to be systematically lower than the DFT values. This is caused by the slight overestimation of the surrogate model on  $\gamma_{\text{usf}}$  for the alloys with relatively low USF energies (Fig. 6a), which is not seen for the predictions of the surface energy (Fig. 6b). This discrepancy should have limited effects on the final results of screening for alloy compositions with enhanced strength-ductility

synergies, because the relative disparity of the  $D$  parameter between different alloys are still generally captured by the surrogate models.

#### 3.4. Screening of the alloy properties in multicomponent systems

Because of our descriptor construction method, the developed surrogate models are able to make immediate predictions on  $\gamma_{\text{usf}}$ ,  $\gamma_{\text{surf}}$  and the  $D$  parameter by only requiring the information of alloy compositions, without the need of any additional DFT calculations. Therefore, the models are quite suitable to perform rapid screenings of these alloy properties in complex compositional spaces. In the present work, we applied the developed surrogate models to systematically screen  $\gamma_{\text{usf}}$  and  $\gamma_{\text{surf}}$  of bcc refractory solid-solution alloys in a multicomponent compositional space to search promising alloy compositions with enhanced strength and ductility. The compositional space chosen for screening is composed of 10 different transition metal elements, which are Ti, Zr, Hf, V, Nb, Ta, Mo, W, Re and Ru. The first 8 elements are commonly included as constituent elements in bcc refractory HEA and multicomponent alloys [8,11]. Re and Ru were also included because these two elements, especially Re, were recognized to improve the low-temperature ductility of Group VI bcc metals under proper alloying amounts [76,77]. In addition, several recent works also reported successful syntheses of novel bcc refractory HEAs that con-

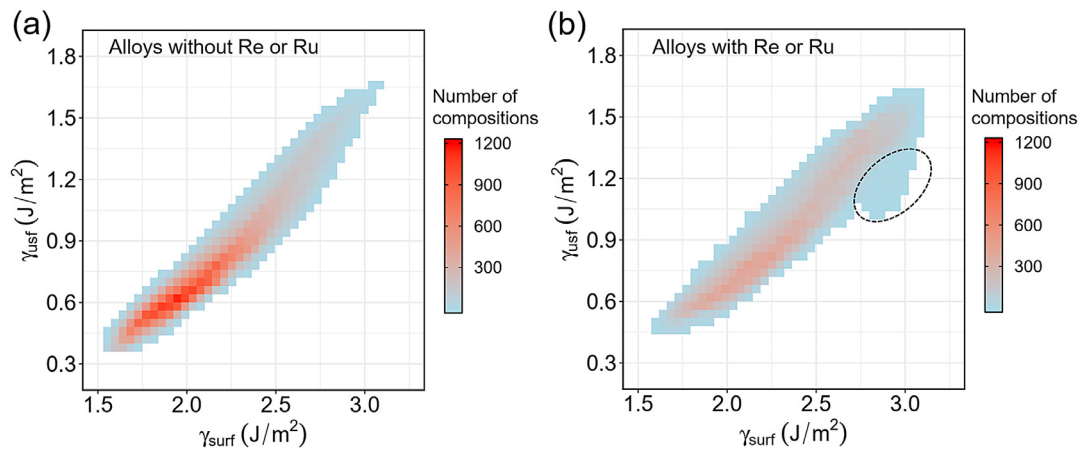


**Fig. 7.** Distribution of the USF ( $\gamma_{\text{usf}}$ ) and surface ( $\gamma_{\text{surf}}$ ) energies predicted by the newly trained surrogate models through the screening of 112,378 quaternary alloys in the 10-component compositional space. (a) Results of the alloys without Re or Ru as constituent elements; (b) Results of the alloys with Re or Ru as constituent elements. A squared unit with a warmer color means that there are more alloy compositions having  $\gamma_{\text{usf}}$  and  $\gamma_{\text{surf}}$  within the coverage area of the unit. The dashed circle in (b) marks a unique distribution pattern of the USF and surface energies from a part of the Re/Ru-containing alloys. The alloys corresponding to the pattern may have strong likelihood of being intrinsically ductile and maintain relatively high mechanical strengths.

taining Re as one of the principle elements [11,78,79]. Therefore, including Re and Ru into the screening space would further expand our theoretical search to cover more unexplored and unconventional alloy compositions in which promising candidates may exist.

Specifically, the screenings were performed over all the quaternary alloy systems in the 10-component space. For each of the quaternary systems, its compositional space was evenly grided using an interval of  $\frac{1}{18}$  mole fraction along each axis that stands for an elemental concentration. The predictions on  $\gamma_{\text{usf}}$  and  $\gamma_{\text{surf}}$  were then performed at individual alloy compositions that correspond to the grid points, and the value of the  $D$  parameter was correspondingly derived based on Eq. 1. Moreover, during the screening, the mole fraction of Re and Ru are constrained to be no more than 0.25 and 0.08333, respectively, by considering their limited binary solubility in the bcc phase of the group V and VI metals [80–82]. The reason that we only screened over all the quaternary systems by a discrete compositional interval is for the convenience of further validations by DFT calculations using SQS supercells. It is known that the necessary supercell size for generating a reliable SQS increases drastically with the number of constituent elements of the system. By applying such screening constraints, any of the screened alloy compositions can be easily accessed by generating a 72-atom SQS supercell. This would allow us to validate the screening results of many different alloy compositions under affordable computational costs. Furthermore, it is worth mentioning that the actual prediction range of the surrogate models is not limited to the quaternary alloys. The models can efficiently predict  $\gamma_{\text{usf}}$  and  $\gamma_{\text{surf}}$  for any multicomponent alloys with continuous compositional variations in the 10-element compositional space.

It has to be emphasized that, to possibly improve the accuracy of the screening results, the surrogate models were further re-trained with all the data in Table 1, instead of splitting the data into training and test sets, and then applied for the screening calculations. The newly trained models would possibly yield more reliable predictions compared with those used for Fig. 6 because the new models included more information on complex multicomponent alloy systems during the training process. Since all the data in Table 1 were employed for training, the predictions of the newly trained models were validated by performing additional DFT calculations with the SQS method as discussed above.

Overall, the newly trained surrogate models have been applied to predict  $\gamma_{\text{usf}}$ ,  $\gamma_{\text{surf}}$  and  $D$  parameters for 112,378 alloy compositions in 210 different quaternary systems. In order to distinguish

the effects of Re and Ru, the prediction results are grouped into two sets for visualization. One of the sets corresponds to the alloys containing Re or Ru, while the other set corresponds to the rest alloys with Re/Ru-free compositions. The distributions of the USF and surface energies from the screening predictions are illustrated in Fig. 7 using 2D density plots, in which a squared unit with a warmer color means that there are more alloy compositions having  $\gamma_{\text{usf}}$  and  $\gamma_{\text{surf}}$  within the coverage area of the unit. As shown in Fig. 7a, in the alloys without Re or Ru, the variations of  $\gamma_{\text{usf}}$  overall exhibits a positive correlation with that of  $\gamma_{\text{surf}}$ . On the other hand, as shown in Fig. 7b, introducing Re or Ru as alloying element leads to a more spread distribution between  $\gamma_{\text{usf}}$  and  $\gamma_{\text{surf}}$ . Particularly, as indicated by the dashed circle in Fig. 7b, the USF and surface energies of a part of Re/Ru-containing alloys show a unique distribution pattern, which is not seen in the results of the Re/Ru-free alloys (Fig. 7a). The alloys corresponding to this pattern generally have surface energies close to the maximum of the screening results but maintain moderate USF energies around  $1.2 \text{ J/m}^2$ , consequently yielding larger  $\frac{\gamma_{\text{surf}}}{\gamma_{\text{usf}}}$  ratios relative to the Re/Ru-free alloys with the same level of USF energies.

The screening results are also visualized by plotting the variations of  $\gamma_{\text{usf}}$  with respect to the  $D$  parameter, as shown in Fig. 8a and 8b for the alloys without or with Re or Ru, respectively. In principle, an alloy with a larger  $\gamma_{\text{usf}}$  could potentially have a higher mechanical strength because higher stress may be required for the dislocation nucleation and motion. Also, based on the Rice criterion of crack-tip deformation [31,32], the alloys with larger  $D$  parameters could have stronger likelihood of being intrinsically ductile. Therefore, the results of Fig. 8 provide qualitative but comprehensive evaluations of the strength-ductility balance of the 112,378 quaternary refractory alloys studied in the screening process. As shown in Fig. 8a and 8b,  $\gamma_{\text{usf}}$  of both the alloys containing and not containing Re or Ru coarsely show negatively nonlinear correlations with the variations of the  $D$  parameter. This result implies that the strength-ductility relationships in the bcc refractory alloys overall follow the classic pattern that alloys with higher mechanical strengths generally should have poorer ductility.

Nevertheless, as shown in Fig. 8a and 8b, the distributions between  $\gamma_{\text{usf}}$  and the  $D$  parameter are also quite dispersed. In other words, the alloys with similar USF energies can still have very different  $D$  parameters, indicating considerable deviations between their ductility performances. Therefore, there are still large degrees of freedom to tune the alloy compositions for optimal strength-ductility synergy. Apparently, the alloys corresponding to the data

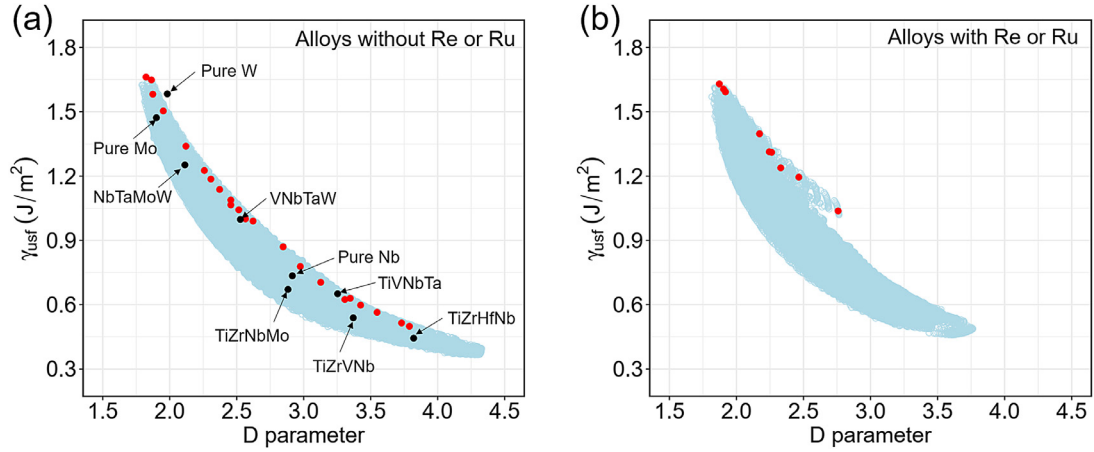


**Fig. 8.** Plots of  $\gamma_{\text{usf}}$  vs. the  $D$  parameter obtained by screening over 112,378 quaternary alloys in the 10-component compositional space. (a) Results of the alloys without Re or Ru as constituent elements; (b) Results of the alloys with Re or Ru as constituent elements. The screening results are represented by the open circles with light-blue color. As a comparison, we also particularly marked the prediction results of some known bcc refractory HEAs and pure bcc metals using solid circles with black color. The data points additionally marked in red correspond to those selected for the DFT validations as listed in Table 3.

on the upper edge of the  $\gamma_{\text{usf}}$  vs.  $D$  parameter distribution should be promising to achieve better strength-ductility synergy, since they have either larger USF energies or values of the  $D$  parameter compared to other alloys with similar  $D$  or USF energy values, respectively.

On the other hand, under the concept of HEAs, many of the previous experimental syntheses on the refractory multicomponent alloys are mainly focused on those with equimolar compositions. As a comparison, we also particularly marked the positions of six previously reported equimolar alloys (i.e., NbTaMoW [7], VNbTaW [83], TiZrNbMo [84], TiVNbTa [85], TiZrVNb [86] and TiZrHfNb [87]) as well as three pure bcc metals (i.e. W, Mo and Nb) on the distribution plot of Fig. 8a. As seen, most of these equimolar alloys are located away from the upper edge of the distribution in Fig. 8a and 8b. This result suggests that there can be other undiscovered alloy compositions, possibly deviated from equimolar, at which we may achieve both mechanical strengths comparable with these known equimolar alloys and improved ductility. These undiscovered alloy compositions can be further rigorously located by an integration of the present surrogate models with other computational models for the predictions of their phase stability, such as the CALPHAD method [11,88,89] and recently developed machine-learning-based and Monte-Carlo-based models [90–95], and accurate mechanical properties [19,21–23,25].

The effects of Re and Ru can be observed by a comparison between Fig. 8a and Fig. 8b. Clearly, the addition of Re or Ru leads to a more spread distribution between  $\gamma_{\text{usf}}$  and the  $D$  parameter, which possibly provides even larger space for optimizing the combination of strength and ductility. Additionally, as shown in Fig. 8b, the  $\gamma_{\text{usf}}$  and  $D$  parameter of a part of the Re/Ru-containing alloys exhibit a different distribution pattern that bows out from the general trend, consistent with the part of the  $\gamma_{\text{usf}}/\gamma_{\text{surf}}$  distribution marked in Fig. 7b. Correspondingly, compared to the Re/Ru-free alloys with similar USF energies, these alloys generally have much higher values of  $D$  parameter, meaning a stronger potency of being intrinsic ductile. The result suggests that the ductility of the bcc refractory multicomponent alloys can be improved without largely trading off the mechanical strength by adding proper amounts of Re or Ru. This argument is also supported by the recent experimental observations [79]. On the other hand, it should also be acknowledged that the cost of Re and Ru may make them only available for niche applications.

Furthermore, it is necessary and valuable to further validate the screening results discussed above using DFT calculations. Specifi-

cally, from the alloy compositions appearing near the upper edge of the  $\gamma_{\text{usf}}$  vs.  $D$  parameter distributions shown in Fig. 8, we randomly selected 25 compositions at which additional DFT calculations with the SQS method were performed to validate the predictions of the surrogate models. Additionally, to further convince the reliability of the surrogate models, we also use DFT calculations to

**Table 3**

Selected alloy compositions, to which additional DFT calculations were performed in order to validate the screening results shown Fig. 8. The superscription, SM, means that the values of  $\gamma_{\text{usf}}$ ,  $\gamma_{\text{surf}}$ , and  $D$  parameter are predicted from the surrogate models, while the superscription, DFT, represents the validation results from the DFT calculations. In the table, the first twenty-five alloys correspond to those appearing near the upper edge of the  $\gamma_{\text{usf}}$  vs.  $D$  parameter distributions shown in Fig. 8, while the last six correspond to the alloy compositions with extreme high  $\gamma_{\text{usf}}$ . The units of  $\gamma_{\text{usf}}$  and  $\gamma_{\text{surf}}$  are J/m<sup>2</sup>.

Alloys	$\gamma_{\text{usf}}^{\text{SM}}$	$\gamma_{\text{surf}}^{\text{SM}}$	$D^{\text{SM}}$	$\gamma_{\text{usf}}^{\text{DFT}}$	$\gamma_{\text{surf}}^{\text{DFT}}$	$D^{\text{DFT}}$
Ti <sub>12</sub> Hf <sub>4</sub> Nb <sub>2</sub> Ta <sub>6</sub>	0.499	1.891	3.789	0.489	1.897	3.880
Ti <sub>13</sub> Hf <sub>2</sub> Nb <sub>4</sub> Ta <sub>5</sub>	0.514	1.919	3.730	0.489	1.899	3.886
Ti <sub>5</sub> Hf <sub>3</sub> V <sub>14</sub> Ta <sub>2</sub>	0.624	2.064	3.307	0.604	2.041	3.379
Ti <sub>8</sub> Hf <sub>2</sub> V <sub>9</sub> Ta <sub>5</sub>	0.598	2.046	3.425	0.532	2.005	3.770
Ti <sub>10</sub> Hf <sub>2</sub> V <sub>2</sub> Ta <sub>10</sub>	0.564	2.001	3.548	0.535	2.014	3.765
Ti <sub>8</sub> V <sub>7</sub> Nb <sub>2</sub> Ta <sub>7</sub>	0.630	2.108	3.347	0.532	2.053	3.859
Ti <sub>3</sub> V <sub>8</sub> Ta <sub>5</sub> W <sub>8</sub>	0.990	2.596	2.622	0.986	2.546	2.583
Ti <sub>4</sub> V <sub>6</sub> Ta <sub>3</sub> W <sub>11</sub>	1.088	2.673	2.456	1.071	2.616	2.444
Ti <sub>2</sub> V <sub>10</sub> Ta <sub>8</sub> W <sub>4</sub>	0.870	2.476	2.846	0.855	2.397	2.804
Ti <sub>4</sub> V <sub>3</sub> Ta <sub>14</sub> W <sub>3</sub>	0.778	2.315	2.975	0.750	2.294	3.060
Hf <sub>3</sub> V <sub>13</sub> Nb <sub>2</sub> Ta <sub>6</sub>	0.704	2.202	3.127	0.607	2.100	3.462
Hf <sub>2</sub> V <sub>7</sub> Nb <sub>4</sub> Ta <sub>11</sub>	1.137	2.699	2.372	1.113	2.631	2.365
Hf <sub>2</sub> W <sub>15</sub> Re <sub>5</sub> Ru <sub>2</sub>	1.238	2.886	2.330	1.236	2.858	2.313
V <sub>2</sub> Mo <sub>10</sub> W <sub>6</sub> Re <sub>6</sub>	1.314	2.949	2.245	1.276	2.931	2.298
V <sub>11</sub> Nb <sub>2</sub> Mo <sub>2</sub> W <sub>9</sub>	1.226	2.769	2.258	1.178	2.664	2.261
V <sub>7</sub> Nb <sub>2</sub> Ta <sub>8</sub> W <sub>7</sub>	1.043	2.623	2.516	1.006	2.569	2.554
V <sub>7</sub> Nb <sub>3</sub> Ta <sub>8</sub> W <sub>6</sub>	1.000	2.566	2.566	0.951	2.508	2.638
V <sub>5</sub> Nb <sub>2</sub> Ta <sub>7</sub> W <sub>10</sub>	1.186	2.737	2.307	1.158	2.700	2.331
V <sub>4</sub> Ta <sub>12</sub> Mo <sub>3</sub> W <sub>5</sub>	1.066	2.617	2.456	1.033	2.592	2.510
V <sub>4</sub> Ta <sub>3</sub> Mo <sub>5</sub> W <sub>12</sub>	1.504	2.935	1.952	1.583	2.952	1.865
V <sub>5</sub> Ta <sub>6</sub> Mo <sub>2</sub> W <sub>11</sub>	1.340	2.842	2.121	1.323	2.841	2.148
V <sub>6</sub> W <sub>11</sub> Re <sub>5</sub> Ru <sub>2</sub>	1.195	2.946	2.465	1.339	2.993	2.236
Ta <sub>2</sub> Mo <sub>3</sub> W <sub>13</sub> Re <sub>6</sub>	1.397	3.036	2.172	1.340	3.022	2.255
Ta <sub>3</sub> W <sub>16</sub> Re <sub>3</sub> Ru <sub>2</sub>	1.311	2.966	2.263	1.320	2.967	2.247
Mo <sub>10</sub> W <sub>6</sub> Re <sub>6</sub> Ru <sub>2</sub>	1.037	2.862	2.758	1.040	2.840	2.731
Ti <sub>2</sub> Nb <sub>2</sub> Mo <sub>3</sub> W <sub>17</sub>	1.582	2.964	1.874	1.639	2.976	1.816
V <sub>2</sub> Ta <sub>2</sub> Mo <sub>2</sub> W <sub>18</sub>	1.649	3.073	1.864	1.749	3.092	1.768
V <sub>2</sub> Ta <sub>3</sub> W <sub>17</sub> Re <sub>2</sub>	1.606	3.057	1.904	1.712	3.100	1.810
Nb <sub>2</sub> Ta <sub>2</sub> Mo <sub>2</sub> W <sub>18</sub>	1.662	3.030	1.823	1.743	3.054	1.752
Nb <sub>2</sub> Ta <sub>2</sub> W <sub>18</sub> Re <sub>2</sub>	1.630	3.052	1.872	1.689	3.070	1.817
Ta <sub>3</sub> Mo <sub>3</sub> W <sub>16</sub> Re <sub>2</sub>	1.593	3.055	1.918	1.632	3.077	1.885

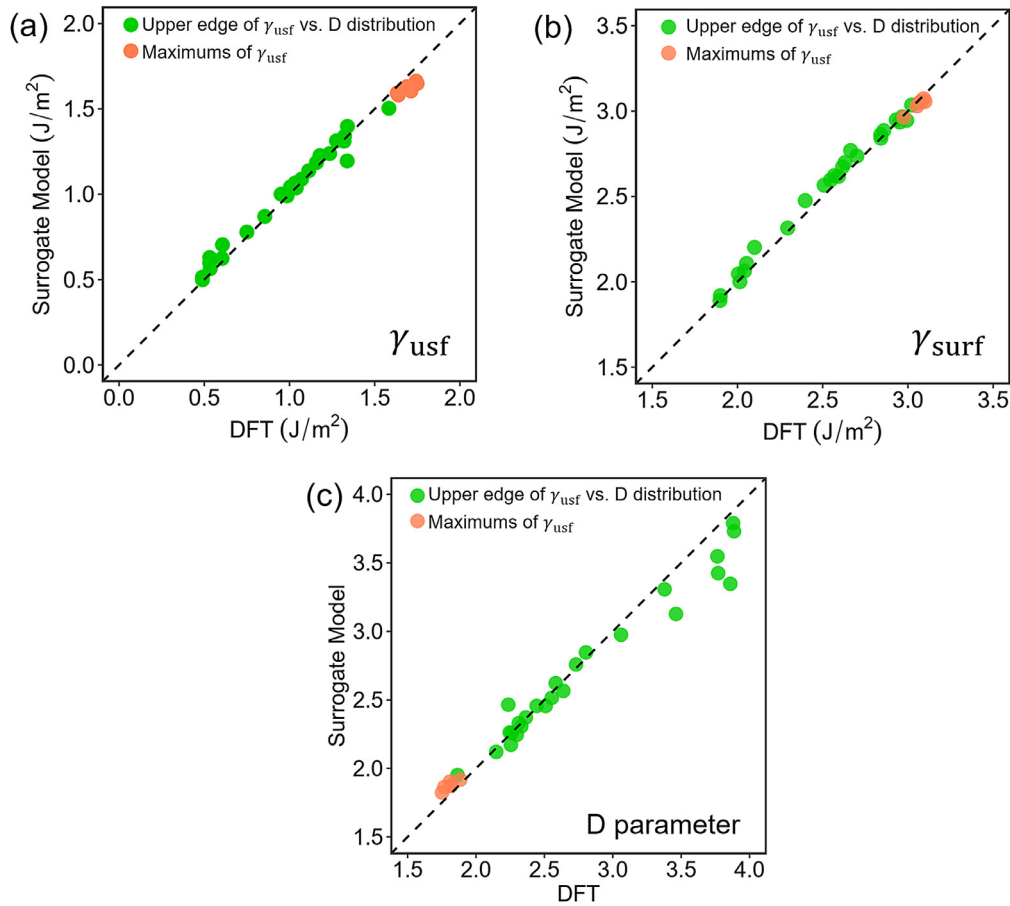


**Fig. 9.** DFT validations of the screening results. The predictions of the surrogate models on (a) unstable stacking fault energy ( $\gamma_{\text{usf}}$ ), (b) surface energy ( $\gamma_{\text{surf}}$ ), and (c)  $D$  parameter are plotted versus the validation results from the DFT calculations. The alloy compositions selected for validation are two sets of data. One set contains 25 samples, marked by green circles, which are randomly selected from the alloy compositions appearing near the upper edge of the  $\gamma_{\text{usf}}$  vs.  $D$  parameter distributions shown in Fig. 8. The other set contains 6 samples, marked by orange circles, randomly selected from the alloy compositions with extreme high  $\gamma_{\text{usf}}$ . More detail are listed in Table 3.

verify a part of the predicted extreme values. More specifically, it is noticed that the surrogate model predicts a few of alloy compositions at which extremely high USF energies can be achieved, even larger than that of pure W as shown in Fig. 8a. Therefore, from these alloy compositions with extreme  $\gamma_{\text{usf}}$ , we also randomly selected 6 compositions for validation. As shown in Fig. 8a and 8b, the locations of the selected alloy compositions on the distributions of  $\gamma_{\text{usf}}$  vs.  $D$  parameter are particularly marked using the solid circles with red color.

For each of the alloy compositions selected for validation, its  $\gamma_{\text{usf}}$ ,  $\gamma_{\text{surf}}$ , and the  $D$  parameter predicted by the DFT calculations are listed in Table 3 along with the predictions from the surrogate models. The validation results are also illustrated as parity plots shown in Fig. 9a, 9b and 9c for  $\gamma_{\text{usf}}$ ,  $\gamma_{\text{surf}}$ , and the  $D$  parameter, respectively. As shown in Fig. 9a and 9b, the predictions of the surrogate models on the USF and surface energies both agree well with the results of the DFT calculations. The corresponding RMSEs are 0.058 and 0.044 J/m², respectively. In terms of the  $D$  parameter, most of the model predictions are in a good agreement with the DFT results (Fig. 9c), though deviations are also observed for a few of alloys with relatively large  $D$  parameters. It should be noted that the surrogate model was never trained by directly using the  $D$  parameter as the fitting response. The predictions on the  $D$  parameter are actually derived from the correspondingly predicted  $\gamma_{\text{usf}}$  and  $\gamma_{\text{surf}}$  based on Eq. 1. Therefore, the predicted  $D$  parameters are influenced by both the prediction uncertainties of  $\gamma_{\text{usf}}$  and  $\gamma_{\text{surf}}$ , consequently having relatively larger errors. Nevertheless, the overall good agreement between the model predictions and DFT

results demonstrates the reliability of the screening results shown in Fig. 7 and 8. The alloy compositions listed in Table 3 could be promising candidates for the future design of bcc refractory multicomponent alloys with an outstanding combination of strength and ductility.

### 3.5. Implication and limitation of the surrogate model for practical alloy designs

There have been many studies to predict the strengths of conventional solid-solution alloys and HEAs based on the GSF values and/or other parameters [19,21–23,25,46], where the comparisons between the model predictions and the experimental results were well discussed. Meanwhile, it is interesting but challenging to verify to what degree the intrinsic ductile potency predicted by the surrogate models can reflect the real ductility of the alloys in practical mechanical tests. As a starting point, we investigated the correlation between the variations of the predicted  $D$  parameter and experimentally measured fracture strains. In principle, a positive correlation shall be expected between the fracture strain and  $D$  parameter since an alloy with a larger  $D$  parameter has a higher likelihood of being intrinsically ductile. Based on a recent review article by O.N. Senkov, et al. [8], we collected a group of experimental data on the room temperature fracture strains of the refractory HEAs that contain the alloying elements studied in the present work. In total 66 measurements were collected, which covered 60 individual alloy compositions, ranging from quaternary to senary systems, as summarized in Table C.1 in Appendix C. We found that



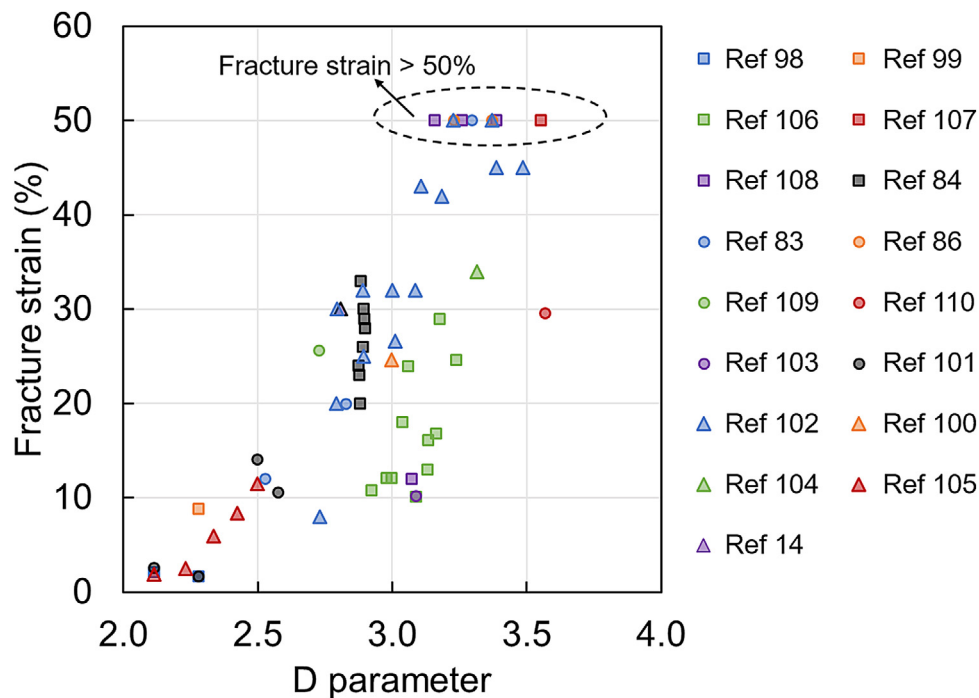


**Fig. 10.** Correlation between the compression fracture strains of some multicomponent bcc refractory alloys and their D parameters predicted by the surrogate models. The fracture strain data were experimental measurements at room temperature and collected from previous literature [14,83,84,86,98–110]. The data points marked by the dashed circle correspond to the alloys for which no macroscopic fracture was observed after 50% compression strain. For each data point, a detailed description on its alloy composition, and the values of the fracture strain and D parameter is shown in Table C.1 in Appendix C.

most of the mechanical tests previously performed on the refractory bcc HEAs were uniaxial compression tests. Then, for each of the collected experimental data, we took its composition to predict the value of the D parameter using our surrogate models.

As shown in Fig. 10, the predicted D parameters indeed show a generally positive correlation with the compression fracture strains for the alloys listed in Table C.1. Particularly, for the alloys with fracture strain over 50% in compression, which are likely to be ductile under tensile deformation, their D parameters are generally larger than those with limited fracture strains. Additionally, there are alloy compositions, namely  $\text{Ti}_{38}\text{Hf}_{24}\text{V}_{15}\text{Nb}_{23}$  [96],  $\text{TiZrHfNbTa}$  [97],  $\text{TiZrHfNb}$  [87], and  $\text{Ti}_{1.5}\text{ZrHf}_{0.5}\text{Nb}_{0.5}\text{Ta}_{0.5}$  [15], at which good tensile ductility was previously measured and reported at room temperature. Correspondingly, we found that the D parameters of these four alloys are around 3.5–3.8, much larger than that of the alloys known to be brittle at room temperature, such as NbMoTaW and VNbMoTaW, which have the D parameters about 2.1–2.2. These results suggest that the predicted D parameter is a useful indicator to qualitatively assess the likelihood of being ductile for the refractory multicomponent alloys studied in the present work.

Furthermore, Fig. 10 also shows that the correlation between the D parameter and fracture strain is qualitative, with relatively large deviations for individual cases. This is not surprising since the fracture behavior of polycrystal materials can hardly be determined by a single parameter but affected by a number of metallurgical factors across scales. Many other important metallurgical factors must be considered and optimized at different length scales. For instance, phase contents are certainly a critical factor to determine alloy's mechanical behaviors. The predictions of the current models were made under the assumption of single-phase alloys, while in practice the single-phase region of the bcc solid-solution phase can be narrower than the screened composition space. For example, the formation of Laves phase (C14 or C15) was generally seen in the refractory alloys with the high contents of Mo and

Zr [8,102]. For the alloys with high contents of group IV elements (usually  $\geq 50$  at%), secondary phases associated with the bcc or hcp structures can nucleate either in the as-cast state [96] or after long-time heat treatment [104]. More importantly, the formation of these secondary phases was found to have significant and versatile effects on both the mechanical strength and ductility of the alloys [8,102,104].

Defects and microstructures are also crucial to the ductility of alloys. It is found that grain boundary (GB) segregation plays an essential role in determining the ductility of bcc refractory alloys. Interstitial elements, such as oxygen and nitrogen, can segregate at GBs during casting and/or annealing and cause GB embrittlement, consequently leading to room-temperature brittleness in some refractory HEAs [111,112]. On the other hand, segregation of Ti was suggested to have a positive impact on GB cohesion in the initially brittle NbMoTaV and NbMoTaVW alloys to result in an improvement in ductility [101,105]. Besides, other than a dislocation-mediated mechanism, the plasticity of some refractory HEAs is also attributed to deformation twinning or strain/stress-induced phase transformation [56–58].

The above arguments demonstrate that the optimization of ductility and strength of the bcc refractory alloys is an important but essentially very complex issue that cannot be addressed by a single model or approach. By taking certain approximations and simplifications, our strategy here is to develop efficient surrogate models to enable rapid screening of the possible alloy compositions with optimized values of  $\gamma_{\text{usf}}$  and  $\frac{\gamma_{\text{surf}}}{\gamma_{\text{usf}}}$  in a large compositional space. We expect our screening results could provide a compositional space that has been significantly narrowed down for practical alloy design, where more rigorous calculations and models, as well as experimental investigation, should be applied with a comprehensive consideration of all the important metallurgical factors. For example, within the framework of the crack-tip fracture model, as we discussed in the introduction section, there are also several important factors worth to be considered for yielding more accurate

predictions on intrinsic ductility. These factors include the effects of elastic constants [26,31], multiplicity of slip and fracture planes [45,46], short-range ordering [49–53], lattice-trapping [54,55], and local fluctuation of composition [48–50]. Moreover, it is worth to point out that the surface energies calculated in present work also have intrinsic uncertainties originated from the self-interaction error in the Kohn-Sham DFT [113–115]. This error can become significant for most approximate exchange-correlation functionals, including the one used in the present work (GGA-PBE) [114], when electron density is approaching to zero. As a result, the total energy calculation of the supercell with a large vacuum region can have larger uncertainties than that of the supercell without vacuum regions, consequently leading to intrinsic errors in the prediction of surface energy. Therefore, the advanced methods [114–116], such as the EXX (exact exchange) + RPA (random phase approximation) method, that yield a better approximation of the electron exchange and correlation to minimize the self-interaction error should be employed in the future for more accurate predictions of surface energy, and so as for the intrinsic ductility. In addition, the CALPHAD-based methods can be utilized to predict the thermodynamic driving forces for the formation of certain intermetallic phases that are detrimental to the ductility [11,88,89].

#### 4. Summary and conclusion

In this work, we developed surrogate models based on statistical regression to effectively and efficiently predict the USF ( $\gamma_{\text{usf}}$ ) and surface ( $\gamma_{\text{surf}}$ ) energies of the  $(\bar{1}10)$  plane in multicomponent bcc solid-solution alloys with constituent elements among Ti, Zr, Hf, V, Nb, Ta, Mo, W, Re and Ru. DFT calculations with the SQS method were performed to compute  $\gamma_{\text{usf}}$  and  $\gamma_{\text{surf}}$  for 106 individual alloy compositions in 14 binary, 3 ternary, and 12 quaternary systems to train and test the surrogate models. From the DFT calculations, it is also found that the variations of  $\gamma_{\text{usf}}$ ,  $\gamma_{\text{surf}}$ , and their ratio in bcc refractory alloys are not well correlated solely with the d-band filling effects. Therefore, using a bond-counting model as an ansatz, a set of descriptors were developed to incorporate not only the filling fraction of d-band but also various features of the chemical bonds and electronic structures of pure metals and ordered intermetallic alloys for the statistical regression of  $\gamma_{\text{usf}}$  and  $\gamma_{\text{surf}}$ . As a result, by only training with the data of binary and ternary alloys, the developed surrogate models can accurately predict  $\gamma_{\text{usf}}$  and  $\gamma_{\text{surf}}$  for multicomponent alloys across a vast compositional space. The models also show the potential capability to extend predictions to cover new types of constituent elements beyond the training data. Furthermore, after comparing with avail-

able experimental data, the model-predicted  $D$  parameter shows a clear and qualitative correlation with the room temperature fracture strains of bulk samples across a wide range of alloy compositions.

Moreover, using the developed surrogate models, a systematic screening of  $\gamma_{\text{usf}}$ ,  $\gamma_{\text{surf}}$  and their ratios (i.e., the  $D$  parameter) were performed over 112,378 quaternary alloy compositions in the 10-element compositional space. As the potency of an alloy being mechanically strong and intrinsically ductile is generally related to its  $\gamma_{\text{usf}}$  and  $D = \frac{\gamma_{\text{surf}}}{\gamma_{\text{usf}}}$ , respectively, the evaluation on the strength-ductility balance of bcc multicomponent refractory alloys was attempted by analyzing the screening results. The results suggest that there could be considerable spaces to tune alloy chemical compositions for further improvements of the strength-ductility synergy relative to the currently known equimolar HEAs. Besides, it is found that introducing Re or Ru can be beneficial to improve the ductility of the multicomponent alloys without largely sacrificing the mechanical strength, although the rareness of the two elements may restrict the applications in practice. Last but not least, the screening results were further confirmed by additional DFT calculations, from which some promising alloy compositions were proposed for future computational and experimental investigations towards the design of bcc refractory multicomponent alloys with enhanced strength and ductility. The codes and trained SL models that support the findings of the present work are available at Materials Commons, (<https://doi.org/10.13011/m3-rkg0-zh65>).

#### Declaration of Competing Interest

The authors declare that they have no known competing financial interests or personal relationships that could have appeared to influence the work reported in this paper.

#### Acknowledgement

This work was supported by the National Science Foundation (NSF) under award DMR-1847837 and the startup fund from the University of Michigan. The calculations were performed by using the Extreme Science and Engineering Discovery Environment (XSEDE) Stampede2 at the TACC through allocation TG-DMR190035. This research was supported in part through computational resources and services provided by Advanced Research Computing Technology Services (ARC-TS), a division of Information and Technology Services (ITS) at the University of Michigan, Ann Arbor. We thank Prof. W. A. Curtin (EPFL) for productive discussions.

## Appendix A. Bond feature parameters and elemental properties for descriptors construction

**Table A1**

A list of bond feature parameters and elemental properties used for descriptor constructions. The bond feature parameters correspond to a group of physical and electronic properties of the bcc pure metals and ordered B2 intermetallics obtained from DFT calculations.

Parameters for descriptors construction		
Bond feature parameters		$E_c^{bcc/b2}$ : cohesive energy $V_{eq}^{bcc/b2}$ : equilibrium atomic volume
	associated with the bulk structure	$\epsilon_{sp}^1(\text{bulk})$ : first order moment of the valence <i>sp</i> -orbital LDOS of the atom in perfect bulk lattice $\epsilon_{sp}^2(\text{bulk})$ : second order moment of the valence <i>sp</i> -orbital LDOS of the atom in perfect bulk lattice $\epsilon_d^1(\text{bulk})$ : first order moment of the valence <i>d</i> -orbital LDOS of the atom in perfect bulk lattice $\epsilon_d^2(\text{bulk})$ : second order moment of the valence <i>d</i> -orbital LDOS of the atom in perfect bulk lattice $dip(\text{bulk})$ : bimodality of the valence <i>d</i> -orbital LDOS of the atom in perfect bulk lattice
	associated with the GSF structure	$\gamma_{usf}^{bcc/b2}$ : the unstable stacking fault energy of the single-element bcc and binary B2 structures $\epsilon_{sp}^1(\text{USF})$ : first order moment of the valence <i>sp</i> -orbital LDOS of the atom on the fault plane $\epsilon_{sp}^2(\text{USF})$ : second order moment of the valence <i>sp</i> -orbital LDOS of the atom on the fault plane $\epsilon_d^1(\text{USF})$ : first order moment of the valence <i>d</i> -orbital LDOS of the atom on the fault plane $\epsilon_d^2(\text{USF})$ : second order moment of the valence <i>d</i> -orbital LDOS of the atom on the fault plane $dip(\text{USF})$ : bimodality of the valence <i>d</i> -orbital LDOS of the atom on the fault plane
	associated with the surface structure	$\gamma_{surf}^{bcc/b2}$ : the surface energy of the single-element bcc and binary B2 structures $\epsilon_{sp}^1(\text{Surf})$ : first order moment of the valence <i>sp</i> -orbital LDOS of the atom on the surface plane $\epsilon_{sp}^2(\text{Surf})$ : second order moment of the valence <i>sp</i> -orbital LDOS of the atom on the surface plane $\epsilon_d^1(\text{Surf})$ : first order moment of the valence <i>d</i> -orbital LDOS of the atom on the surface plane $\epsilon_d^2(\text{Surf})$ : second order moment of the valence <i>d</i> -orbital LDOS of the atom on the surface plane $dip(\text{Surf})$ : bimodality of the valence <i>d</i> -orbital LDOS of the atom on the surface plane
Elemental properties		$\chi$ : electronegativity by Pauling scale $N_{val}$ : number of valence electrons

Appendix B. Details of  $\gamma_{\text{usf}}$  and  $\gamma_{\text{surf}}$  of the alloys listed in Table B1**Table B1**

$\gamma_{\text{usf}}$  and  $\gamma_{\text{surf}}$  predicted from the DFT calculations and the surrogate models for the binary, ternary and quaternary refractory alloys listed in Table 1. The superscription, DFT, means that the values of  $\gamma_{\text{usf}}$ ,  $\gamma_{\text{surf}}$ , and D parameter are obtained by the DFT calculations with the SQS method, while the superscription, SM, represents the values predicted from the surrogate models. The units of  $\gamma_{\text{usf}}$  and  $\gamma_{\text{surf}}$  are J/m<sup>2</sup>. The plots of Fig. 5 and 6 can be reproduced by the data listed here.

Alloys	$\gamma_{\text{usf}}^{\text{SM}}$	$\gamma_{\text{surf}}^{\text{SM}}$	$D^{\text{SM}}$	$\gamma_{\text{usf}}^{\text{DFT}}$	$\gamma_{\text{surf}}^{\text{DFT}}$	$D^{\text{DFT}}$
Ti <sub>3</sub> Nb	0.483	1.839	3.812	0.438	1.856	4.253
Ti <sub>2</sub> Nb	0.502	1.861	3.709	0.449	1.849	4.140
TiNb	0.546	1.912	3.500	0.488	1.905	3.889
TiNb <sub>2</sub>	0.600	1.974	3.292	0.534	1.951	3.651
TiNb <sub>3</sub>	0.631	2.012	3.188	0.562	1.993	3.537
Ti <sub>3</sub> W	0.678	2.066	3.049	0.612	2.042	3.313
Ti <sub>2</sub> W	0.751	2.155	2.868	0.687	2.134	3.104
TiW	0.932	2.380	2.553	0.906	2.387	2.632
TiW <sub>2</sub>	1.199	2.699	2.252	1.180	2.688	2.279
TiW <sub>3</sub>	1.370	2.845	2.077	1.360	2.838	2.082
TiW <sub>7</sub>	1.605	3.052	1.902	1.671	3.062	1.833
Ti <sub>3</sub> Ru	0.716	1.965	2.746	0.690	1.972	2.860
Ti <sub>2</sub> Ru	0.805	2.042	2.537	0.731	2.042	2.795
TiRu	0.852	2.166	2.543	0.778	2.129	2.736
Hf <sub>3</sub> Nb	0.508	1.730	3.407	0.496	1.731	3.485
Hf <sub>2</sub> Nb	0.526	1.761	3.350	0.505	1.794	3.500
HfNb	0.562	1.836	3.263	0.516	1.835	3.521
HfNb <sub>2</sub>	0.610	1.925	3.155	0.563	1.890	3.294
HfNb <sub>3</sub>	0.642	1.979	3.083	0.591	1.926	3.243
V <sub>7</sub> W	0.889	2.519	2.835	0.851	2.535	2.980
V <sub>3</sub> W	0.992	2.641	2.661	0.985	2.663	2.704
VW	1.276	2.878	2.255	1.291	2.898	2.246
VW <sub>3</sub>	1.572	3.079	1.959	1.687	3.097	1.836
VW <sub>7</sub>	1.689	3.152	1.866	1.792	3.178	1.773
Nb <sub>7</sub> Ta	0.753	2.204	2.929	0.710	2.136	3.009
Nb <sub>3</sub> Ta	0.751	2.191	2.919	0.719	2.160	3.006
NbTa	0.749	2.209	2.950	0.733	2.223	3.032
NbTa <sub>3</sub>	0.748	2.225	2.975	0.734	2.276	3.100
NbTa <sub>7</sub>	0.748	2.228	2.980	0.732	2.304	3.146
Nb <sub>3</sub> Mo	0.973	2.320	2.385	0.949	2.304	2.423
Nb <sub>2</sub> Mo	1.051	2.381	2.266	1.040	2.383	2.289
NbMo	1.222	2.517	2.060	1.235	2.518	2.038
NbMo <sub>2</sub>	1.367	2.646	1.936	1.416	2.648	1.869
NbMo <sub>3</sub>	1.420	2.699	1.901	1.461	2.691	1.839
Nb <sub>3</sub> W	0.986	2.387	2.420	0.961	2.368	2.461
Nb <sub>2</sub> W	1.079	2.481	2.300	1.054	2.467	2.338
NbW	1.304	2.675	2.052	1.292	2.681	2.076
NbW <sub>2</sub>	1.531	2.878	1.880	1.569	2.890	1.841
NbW <sub>3</sub>	1.625	2.969	1.827	1.668	2.966	1.775
Nb <sub>7</sub> Ru	0.881	2.195	2.490	0.888	2.237	2.518
Nb <sub>3</sub> Ru	0.918	2.238	2.439	0.945	2.273	2.404
Nb <sub>2</sub> Ru	0.887	2.256	2.544	0.943	2.298	2.436
NbRu	0.786	2.288	2.910	0.760	2.299	3.023
Ta <sub>7</sub> Mo	0.871	2.379	2.730	0.849	2.417	2.845
Ta <sub>3</sub> Mo	0.965	2.469	2.557	0.969	2.492	2.572
TaMo	1.203	2.625	2.182	1.238	2.650	2.141
TaMo <sub>3</sub>	1.461	2.751	1.882	1.500	2.766	1.843
TaMo <sub>7</sub>	1.504	2.795	1.859	1.503	2.780	1.850
Ta <sub>7</sub> Re	0.957	2.503	2.616	0.943	2.507	2.657
Ta <sub>3</sub> Re	1.180	2.652	2.247	1.172	2.650	2.261
TaRe	1.568	2.857	1.822	1.685	2.878	1.707
TaRe <sub>3</sub>	1.081	2.850	2.638	0.975	2.779	2.850
Mo <sub>7</sub> W	1.422	2.855	2.008	1.458	2.835	1.945
Mo <sub>3</sub> W	1.461	2.904	1.987	1.495	2.883	1.928
MoW	1.530	3.002	1.962	1.561	2.981	1.910
MoW <sub>3</sub>	1.585	3.083	1.945	1.627	3.089	1.899
MoW <sub>7</sub>	1.606	3.117	1.940	1.660	3.149	1.897
W <sub>7</sub> Re	1.473	3.143	2.133	1.489	3.186	2.140

(continued on next page)



**Table B1**  
(continued)

Alloys	$\gamma_{\text{usf}}^{\text{SM}}$	$\gamma_{\text{surf}}^{\text{SM}}$	$D^{\text{SM}}$	$\gamma_{\text{usf}}^{\text{DFT}}$	$\gamma_{\text{surf}}^{\text{DFT}}$	$D^{\text{DFT}}$
W <sub>3</sub> Re	1.309	3.094	2.364	1.318	3.123	2.369
WRe	1.049	2.967	2.830	1.025	3.008	2.928
WRe <sub>3</sub>	0.887	2.853	3.216	0.929	2.790	3.020
W <sub>7</sub> Ru	1.288	3.021	2.346	1.307	3.057	2.339
W <sub>3</sub> Ru	1.091	2.833	2.598	1.111	2.817	2.505
W <sub>2</sub> Ru	1.004	2.717	2.705	0.962	2.725	2.828
Ti <sub>2</sub> NbW	0.736	2.124	2.885	0.723	2.094	3.104
Ti <sub>2</sub> Nb <sub>2</sub> W	0.740	2.121	2.868	0.733	2.099	3.182
TiNbW	0.870	2.263	2.600	0.865	2.261	2.758
TiNb <sub>2</sub> W	0.848	2.232	2.633	0.859	2.223	2.705
TiNb <sub>2</sub> W <sub>2</sub>	1.004	2.414	2.404	0.955	2.388	2.500
TiNbW <sub>2</sub>	1.066	2.516	2.361	1.086	2.498	2.399
TiWRe	1.337	2.752	2.058	1.403	2.768	1.973
TiW <sub>2</sub> Re	1.385	2.853	2.060	1.509	2.902	1.924
TiNbRu	0.903	2.201	2.437	0.847	2.109	2.492
TiNb <sub>2</sub> Ru	0.896	2.193	2.447	0.905	2.189	2.418
TiZrHfNb	0.430	1.718	3.992	0.464	1.731	3.732
TiZrHf <sub>2</sub> Nb <sub>2</sub>	0.466	1.749	3.750	0.476	1.733	3.642
TiZrHfNb <sub>3</sub>	0.526	1.826	3.470	0.506	1.787	3.531
TiZrVNb	0.526	1.852	3.520	0.496	1.814	3.660
TiZr <sub>2</sub> V <sub>2</sub> Nb	0.523	1.826	3.491	0.520	1.787	3.439
TiVNbMo	0.826	2.216	2.685	0.783	2.182	2.788
TiNbWRe	1.218	2.616	2.147	1.250	2.598	2.078
TiNb <sub>3</sub> WRe	1.085	2.452	2.260	1.025	2.423	2.364
TiNb <sub>2</sub> W <sub>2</sub> Re	1.232	2.628	2.132	1.246	2.624	2.106
TiNbW <sub>3</sub> Re	1.370	2.818	2.057	1.453	2.816	1.938
TiNbWRu	1.056	2.370	2.245	1.057	2.399	2.269
TiNb <sub>3</sub> WRu	0.999	2.311	2.313	0.952	2.340	2.457
TiNb <sub>2</sub> W <sub>2</sub> Ru	1.122	2.434	2.169	1.106	2.489	2.250
TiNbW <sub>3</sub> Ru	1.204	2.597	2.156	1.223	2.660	2.175
VNbWRu	1.085	2.490	2.295	1.093	2.561	2.342
VNb <sub>2</sub> W <sub>2</sub> Ru	1.177	2.529	2.149	1.193	2.604	2.182
VNbW <sub>3</sub> Ru	1.208	2.728	2.259	1.257	2.756	2.192
VMoWRu	1.054	2.625	2.491	1.107	2.722	2.460
VMoW <sub>3</sub> Ru	1.156	2.820	2.439	1.230	2.849	2.316
Nb <sub>2</sub> Ta <sub>2</sub> MoW	1.056	2.487	2.354	1.031	2.492	2.416
NbTaMoW	1.231	2.638	2.143	1.264	2.661	2.106
NbTa <sub>3</sub> MoW	1.054	2.519	2.390	1.047	2.540	2.425
NbTaMoW <sub>3</sub>	1.458	2.844	1.951	1.546	2.867	1.854
Nb <sub>3</sub> TaWRu	1.100	2.379	2.162	1.107	2.471	2.233
Nb <sub>2</sub> TaW <sub>2</sub> Ru	1.207	2.493	2.065	1.215	2.596	2.137
NbMoW <sub>3</sub> Ru	1.182	2.763	2.338	1.199	2.753	2.296
Ta <sub>2</sub> MoW <sub>2</sub> Re	1.484	2.875	1.937	1.576	2.918	1.851
TaMoWRe	1.454	2.922	2.010	1.450	2.898	1.998
TaMoW <sub>3</sub> Re	1.504	3.006	1.999	1.520	2.994	1.970
TaMoWRu	1.144	2.565	2.243	1.041	2.629	2.525
TaMo <sub>2</sub> W <sub>2</sub> Ru	1.193	2.707	2.268	1.186	2.730	2.301
TaMoW <sub>3</sub> Ru	1.226	2.777	2.265	1.226	2.808	2.290

**Appendix C. Experimental fracture strains of some multicomponent bcc refractory alloys in comparison the predicted D parameter****Table C1**

Experimental fracture strains and predicted *D* parameter of some multicomponent bcc refractory alloys at room temperature. The experimental data were collected from previous literature [14,15,83,84,86,87,96–110].

Alloys	Ref	Mechanical Testing	Fracture Strain (%)	D parameter
NbTaMoW	[98]	Compression	2.1	2.113
VNbTaMoW	[98]	Compression	1.7	2.280
VNbTaMoW	[99]	Compression	8.8	2.280
TiZrHfNbMo	[106]	Compression	10.12	3.088
TiZrHfNb <sub>0.5</sub> Mo	[106]	Compression	13.02	3.13
TiZrHfNb <sub>1.5</sub> Mo	[106]	Compression	23.97	3.058
Ti <sub>0.5</sub> ZrHfNbMo	[106]	Compression	12.08	2.979
Ti <sub>1.5</sub> ZrHfNbMo	[106]	Compression	28.98	3.177
TiZr <sub>0.5</sub> HfNbMo	[106]	Compression	18.02	3.038
TiZr <sub>1.5</sub> HfNbMo	[106]	Compression	16.09	3.135
TiZrHf <sub>0.5</sub> NbMo	[106]	Compression	12.09	2.997
TiZrHf <sub>1.5</sub> NbMo	[106]	Compression	16.83	3.162
TiZrHf <sub>0.5</sub> NbMo <sub>0.5</sub>	[106]	Compression	24.61	3.237
TiZrHfNbMo <sub>1.5</sub>	[106]	Compression	10.83	2.924
TiZrHfNbTa	[107]	Compression	>50	3.552
TiZrHfNbTa	[108]	Compression	>50	3.552
TiZrHfNbTaMo <sub>0.25</sub>	[108]	Compression	>50	3.388
TiZrHfNbTaMo <sub>0.5</sub>	[108]	Compression	>50	3.26
TiZrHfNbTaMo <sub>0.75</sub>	[108]	Compression	>50	3.158
TiZrHfNbTaMo	[108]	Compression	12	3.073
TiZrNbMo	[84]	Compression	33	2.883
TiZrV <sub>0.25</sub> NbMo	[84]	Compression	30	2.893
TiZrV <sub>0.5</sub> NbMo	[84]	Compression	28	2.898
TiZrV <sub>0.75</sub> NbMo	[84]	Compression	29	2.896
TiZrVNbMo	[84]	Compression	26	2.890
TiZrV <sub>1.5</sub> NbMo	[84]	Compression	20	2.881
TiZrV <sub>2</sub> NbMo	[84]	Compression	23	2.877
TiZrV <sub>3</sub> NbMo	[84]	Compression	24	2.874
TiVNbTa	[83]	Compression	>50	3.296
TiVNbTaW	[83]	Compression	20	2.827
NbTaVW	[83]	Compression	12	2.527
TiZrVNb	[86]	Compression	>50	3.370
TiZrV <sub>2</sub> Nb	[86]	Compression	>50	3.230
TiVNbMo	[109]	Compression	25.62	2.728
TiZrHfVNb	[110]	Compression	29.6	3.569
TiZrHfNbMo	[103]	Compression	10.2	3.088
TiVNbTaMoW	[101]	Compression	10.6	2.575
TiNbTaMoW	[101]	Compression	14.1	2.498
NbTaMoW	[101]	Compression	2.6	2.113
VNbTaMoW	[101]	Compression	1.7	2.280
TiZrVNb	[102]	Compression	>50	3.370
TiZrV <sub>0.3</sub> Nb	[102]	Compression	45	3.485
TiZrVNbMo <sub>0.3</sub>	[102]	Compression	42	3.185
TiZrVNbMo <sub>0.5</sub>	[102]	Compression	32	3.085
TiZrVNbMo <sub>0.7</sub>	[102]	Compression	32	3.000
TiZrVNbMo	[102]	Compression	32	2.890
TiZrVNbMo <sub>1.3</sub>	[102]	Compression	30	2.795
TiZrV <sub>0.3</sub> NbMo <sub>0.1</sub>	[102]	Compression	45	3.387
TiZrV <sub>0.3</sub> NbMo <sub>0.3</sub>	[102]	Compression	>50	3.226
TiZrV <sub>0.3</sub> NbMo <sub>0.5</sub>	[102]	Compression	43	3.106
TiZrV <sub>0.3</sub> NbMo <sub>0.7</sub>	[102]	Compression	26.6	3.011
TiZrV <sub>0.3</sub> NbMo <sub>1.0</sub>	[102]	Compression	25	2.894
TiZrV <sub>0.3</sub> NbMo <sub>1.3</sub>	[102]	Compression	20	2.793
TiZrV <sub>0.3</sub> NbMo <sub>1.5</sub>	[102]	Compression	8	2.731
TiZrHf <sub>0.5</sub> NbMo <sub>0.5</sub>	[100]	Compression	24.61	2.997
ZrHfNbTa	[104]	Compression	34	3.316
NbTaMoW	[105]	Compression	1.9	2.113
Ti <sub>0.25</sub> NbTaMoW	[105]	Compression	2.5	2.233
Ti <sub>0.5</sub> NbTaMoW	[105]	Compression	5.9	2.335
Ti <sub>0.75</sub> NbTaMoW	[105]	Compression	8.4	2.424
TiNbTaMoW	[105]	Compression	11.5	2.498
TiVNbTaMo	[14]	Compression	30	2.809
Ti <sub>38</sub> Hf <sub>24</sub> V <sub>15</sub> Nb <sub>23</sub>	[96]	Tension	20.6	3.713
TiZrHfNbTa	[97]	Tension	9.7	3.552
TiZrHfNb	[87]	Tension	14.9	3.821
Ti <sub>1.5</sub> ZrHf <sub>0.5</sub> Nb <sub>0.5</sub> Ta <sub>0.5</sub>	[15]	Tension	18.8	3.817

## References

- [1] A. Sutton, *Electronic structure of materials*, Clarendon Press, 1993.
- [2] D. Brunner, Comparison of flow-stress measurements on high-purity tungsten single crystals with the kink-pair theory, *Materials Transactions, JIM* 41 (1) (2000) 152–160.
- [3] S. Takeuchi, K. Maeda, Slip in high purity tantalum between 0.7 and 40K, *Acta metallurgica* 25 (12) (1977) 1485–1490.
- [4] T. Suzuki, Y. Kamimura, H. Kirchner, Plastic homology of bcc metals, *Philosophical Magazine A* 79 (7) (1999) 1629–1642.
- [5] L. Dezerald, L. Ventelon, E. Clouet, C. Denoual, D. Rodney, F. Willaime, Ab initio modeling of the two-dimensional energy landscape of screw dislocations in bcc transition metals, *Physical Review B* 89 (2) (2014) 024104.
- [6] E. Savitskii, *Physical metallurgy of refractory metals and alloys*, Springer Science & Business Media, 2012.
- [7] O. Senkov, G. Wilks, D. Miracle, C. Chuang, P. Liaw, Refractory high-entropy alloys, *Intermetallics* 18 (9) (2010) 1758–1765.
- [8] O. Senkov, D.B. Miracle, K. Chaput, J.-P. Couzinie, Development and exploration of refractory high entropy alloys A review, *Journal of materials research* 33 (19) (2018) 3092–3128.
- [9] V. Soni, B. Gwalani, T. Alam, S. Dasari, Y. Zheng, O. Senkov, D. Miracle, R. Banerjee, Phase inversion in a two-phase, BCC+ B2, refractory high entropy alloy, *Acta Materialia* 185 (2020) 89–97.
- [10] C. Lee, G. Song, M. Gao, R. Feng, P. Chen, J. Brechtel, Y. Chen, K. An, W. Guo, J. Poplawsky, Lattice distortion in a strong and ductile refractory high-entropy alloy, *Acta Materialia* 160 (2018) 158–172.
- [11] M. Gao, Design of high-entropy alloys, in: *High-Entropy Alloys*, Springer, 2016, pp. 369–398.
- [12] M. Gao, P. Gao, J. Hawk, L. Ouyang, D. Alman, M. Widom, Computational modeling of high-entropy alloys: Structures, thermodynamics and elasticity, *Journal of Materials Research* 32 (19) (2017) 3627–3641.
- [13] O. Senkov, S. Gorsse, D. Miracle, High temperature strength of refractory complex concentrated alloys, *Acta Materialia* 175 (2019) 394–405.
- [14] H. Yao, J. Qiao, J. Hawk, H. Zhou, M. Chen, M. Gao, Mechanical properties of refractory high-entropy alloys: Experiments and modeling, *Journal of Alloys and Compounds* 696 (2017) 1139–1150.
- [15] S. Sheikhi, S. Shafeie, Q. Hu, J. Ahlström, C. Persson, J. Veselý, J. Zýka, U. Klemment, S. Guo, Alloy design for intrinsically ductile refractory high-entropy alloys, *Journal of applied physics* 120 (16) (2016) 164902.
- [16] F. Coury, M. Kaufman, A. Clarke, Solid-solution strengthening in refractory high entropy alloys, *Acta Materialia* 175 (2019) 66–81.
- [17] P. Shi, W. Ren, T. Zheng, Z. Ren, X. Hou, J. Peng, P. Hu, Y. Gao, Y. Zhong, P. Liaw, Enhanced strength–ductility synergy in ultrafine-grained eutectic high-entropy alloys by inheriting microstructural lamellae, *Nature communications* 10 (1) (2019) 1–8.
- [18] Y. Zhang, T. Zuo, Z. Tang, M. Gao, K. Dahmen, P. Liaw, Z. Lu, Microstructures and properties of high-entropy alloys, *Progress in Materials Science* 61 (2014) 1–93.
- [19] S. Rao, E. Antillon, C. Woodward, B. Akdim, T. Parthasarathy, O. Senkov, Solution hardening in body-centered cubic quaternary alloys interpreted using suzuki's kink-solute interaction model, *Scripta Materialia* 165 (2019) 103–106.
- [20] C. Varvenne, A. Luque, W. Curtin, Theory of strengthening in fcc high entropy alloys, *Acta Materialia* 118 (2016) 164–176.
- [21] B. Yin, F. Maresca, W. Curtin, Vanadium is an optimal element for strengthening in both fcc and bcc high-entropy alloys, *Acta Materialia* 188 (2020) 486–491.
- [22] F. Maresca, W. Curtin, Mechanistic origin of high strength in refractory BCC high entropy alloys up to 1900K, *Acta Materialia* 182 (2020) 235–249.
- [23] E. George, W. Curtin, C. Tasan, High entropy alloys: A focused review of mechanical properties and deformation mechanisms, *Acta Materialia* 188 (2020) 435–474.
- [24] C. LaRosa, M. Shih, C. Varvenne, M. Ghazisaeidi, Solid solution strengthening theories of high-entropy alloys, *Materials Characterization* 151 (2019) 310–317.
- [25] S. Rao, C. Varvenne, C. Woodward, T. Parthasarathy, D. Miracle, O. Senkov, W. Curtin, Atomistic simulations of dislocations in a model BCC multicomponent concentrated solid solution alloy, *Acta Materialia* 125 (2017) 311–320.
- [26] X. Li, W. Li, D. Irving, L. Varga, L. Vitos, S. Schönecker, Ductile and brittle crack-tip response in equimolar refractory high-entropy alloys, *Acta Materialia* (2020).
- [27] S. Pugh, Xcii. relations between the elastic moduli and the plastic properties of polycrystalline pure metals, *The London, Edinburgh, and Dublin Philosophical Magazine and Journal of Science* 45 (367) (1954) 823–843.
- [28] L. Qi, D. Chrzan, Tuning ideal tensile strengths and intrinsic ductility of bcc refractory alloys, *Physical review letters* 112 (11) (2014) 115503.
- [29] C. Yang, L. Qi, Ab initio calculations of ideal strength and lattice instability in W-Ta and W-Re alloys, *Physical Review B* 97 (1) (2018) 014107.
- [30] I. Winter, M. de Jong, J. Montoya, E. Rothchild, D. Chrzan, Intrinsic ductility of random substitutional alloys from nonlinear elasticity theory, *Physical Review Materials* 3 (11) (2019) 113608.
- [31] J. Rice, R. Thomson, Ductile versus brittle behaviour of crystals, *The Philosophical Magazine: A Journal of Theoretical Experimental and Applied Physics* 29 (1) (1974) 73–97.
- [32] J. Rice, Dislocation nucleation from a crack tip: an analysis based on the Peierls concept, *Journal of the Mechanics and Physics of Solids* 40 (2) (1992) 239–271.
- [33] M. Mehl, D. Papaconstantopoulos, N. Kioussis, M. Herbranson, Tight-binding study of stacking fault energies and the Rice criterion of ductility in the fcc metals, *Physical Review B* 61 (2000) 4894–4897.
- [34] Z. Wu, W. Curtin, Brittle and ductile crack-tip behavior in magnesium, *Acta Materialia* 88 (2015) 1–12.
- [35] P. Andric, W. Curtin, New theory for Mode I crack-tip dislocation emission, *Journal of the Mechanics and Physics of Solids* 106 (2017) 315–337.
- [36] T. Zhu, J. Li, S. Yip, Atomistic study of dislocation loop emission from a crack tip, *Physical review letters* 93 (2) (2004) 025503.
- [37] A. Van De Walle, P. Tiwary, M. De Jong, D. Olmsted, M. Asta, A. Dick, D. Shin, Y. Wang, L. Chen, Z. Liu, Efficient stochastic generation of special quasirandom structures, *Calphad: Computer Coupling of Phase Diagrams and Thermochemistry* 42 (2013) 13–18, doi:10.1016/j.calphad.2013.06.006.
- [38] M. de Jong, L. Qi, D. Olmsted, A. van de Walle, M. Asta, Calculations of planar defect energies in substitutional alloys using the special-quasirandom-structure approach, *Physical Review B* 93 (9) (2016) 094101.
- [39] M. De Jong, J. Kacher, M. Sluiter, L. Qi, D. Olmsted, A. Van De Walle, J. Morris, A. Minor, M. Asta, Electronic origins of anomalous twin boundary energies in hexagonal close packed transition metals, *Physical Review Letters* 115 (6) (2015) 065501, doi:10.1103/PhysRevLett.115.065501.
- [40] S. Zhao, G. Stocks, Y. Zhang, Stacking fault energies of face-centered cubic concentrated solid solution alloys, *Acta Materialia* 134 (2017) 334–345.
- [41] C. Niu, C. LaRosa, J. Miao, M. Mills, M. Ghazisaeidi, Magnetically-driven phase transformation strengthening in high entropy alloys, *Nature communications* 9 (1) (2018) 1–9.
- [42] S. Xu, E. Hwang, W. Jian, Y. Su, I. Beyerlein, Atomistic calculations of the generalized stacking fault energies in two refractory multi-principal element alloys, *Intermetallics* 124 (2020) 106844.
- [43] Y. Hu, G. Zhao, B. Zhang, C. Yang, M. Zhang, Z. Liu, X. Qian, L. Qi, Local electronic descriptors for solute-defect interactions in bcc refractory metals, *Nature communications* 10 (1) (2019) 1–11.
- [44] H. Mao, H. Chen, Q. Chen, TCHEAT: A thermodynamic database not limited for high entropy alloys, *Journal of Phase Equilibria and Diffusion* 38 (4) (2017) 353–368.
- [45] F. Wang, G. Balbus, S. Xu, Y. Su, J. Shin, P. Rottmann, K. Knipling, J.-C. Stinville, L. Mills, O. Senkov, I. Beyerlein, T. Pollock, D. Gianola, Multiplicity of dislocation pathways in a refractory multiprincipal element alloy, *Science* 370 (6512) (2020) 95–101, doi:10.1126/science.aba3722.
- [46] S. Xu, Y. Su, W. Jian, I. Beyerlein, Local slip resistances in equal-molar MoNbTi multi-principal element alloy, *Acta Materialia* 202 (2021) 68–79, doi:10.1016/j.actamat.2020.10.042.
- [47] G. Kim, H. Diao, C. Lee, A. Samaei, T. Phan, M. de Jong, K. An, D. Ma, P. Liaw, W. Chen, First-principles and machine learning predictions of elasticity in severely lattice-distorted high-entropy alloys with experimental validation, *Acta Materialia* 181 (2019) 124–138.
- [48] J. Ding, Q. Yu, M. Asta, R. Ritchie, Tunable stacking fault energies by tailoring local chemical order in CrCoNi medium-entropy alloys, *Proceedings of the National Academy of Sciences* 115 (36) (2018) 8919–8924.
- [49] Q. Li, H. Sheng, E. Ma, Strengthening in multi-principal element alloys with local-chemical-order roughened dislocation pathways, *Nature communications* 10 (1) (2019) 1–11.
- [50] A. Natarajan, A. Van der Ven, Linking electronic structure calculations to generalized stacking fault energies in multicomponent alloys, *npj Computational Materials* 6 (1) (2020) 80, doi:10.1038/s41524-020-0348-z.
- [51] R. Zhang, S. Zhao, J. Ding, Y. Chong, T. Jia, C. Ophus, M. Asta, R. Ritchie, A. Minor, Short-range order and its impact on the CrCoNi medium-entropy alloy, *Nature* 581 (7808) (2020) 283–287.
- [52] P. Singh, A. Sharma, A. Smirnov, M. Djalio, P. Ray, G. Balasubramanian, D. Johnson, Design of high-strength refractory complex solid-solution alloys, *npj Computational Materials* 4 (1) (2018) 1–8.
- [53] X. Li, C. Chen, H. Zheng, Y. Zuo, S. Ong, Complex strengthening mechanisms in the NbMoTaW multi-principal element alloy, *npj Computational Materials* 6 (1) (2020) 1–10.
- [54] W. Curtin, On lattice trapping of cracks, *Journal of Materials Research* 5 (1990) 1549–1560.
- [55] P. Gumbsch, Brittle fracture and the brittle-to-ductile transition of tungsten, *Journal of Nuclear Materials* 323 (2003) 304–312.
- [56] O. Senkov, J. Scott, S. Senkova, F. Meisenkothen, D. Miracle, C. Woodward, Microstructure and elevated temperature properties of a refractory TaNbHfZrTi alloy, *Journal of Materials Science* 47 (9) (2012) 4062–4074.
- [57] J.-P. Couzinie, L. Liliensten, Y. Champion, G. Dirras, L. Perrière, I. Guillot, On the room temperature deformation mechanisms of a TiZrHfNbTa refractory high-entropy alloy, *Materials Science and Engineering: A* 645 (2015) 255–263.
- [58] L. Liliensten, J.-P. Couzinie, J. Bourgon, L. Perrière, G. Dirras, F. Prima, I. Guillot, Design and tensile properties of a bcc Ti-rich high-entropy alloy with transformation-induced plasticity, *Materials Research Letters* 5 (2) (2017) 110–116.
- [59] S. Ogata, J. Li, S. Yip, Energy landscape of deformation twinning in bcc and fcc metals, *Physical Review B* 71 (22) (2005) 224102.
- [60] A. Zunger, S. Wei, L. Ferreira, J. Bernard, Special quasirandom structures, *Physical Review Letters* 65 (3) (1990) 353.
- [61] P. Tu, Y. Zheng, C. Zhuang, X. Zeng, H. Zhu, A high-throughput computation framework for generalized stacking fault energies of pure metals, *Computational Materials Science* 159 (2019) 357–364.
- [62] G. Kresse, J. Furthmüller, Efficient iterative schemes for ab initio total-energy calculations using a plane-wave basis set, *Physical Review B* 54 (16) (1996) 11169.

- [63] P. Blöchl, Projector augmented-wave method, *Phys. Rev. B* 50 (24) (1994) 17953–17979, doi:10.1103/PhysRevB.50.17953.
- [64] J. Perdew, K. Burke, M. Ernzerhof, Generalized gradient approximation made simple, *Physical Review Letters* 77 (18) (1996) 3865–3868, doi:10.1103/PhysRevLett.77.3865.
- [65] M. De Jong, W. Chen, R. Notestine, K. Persson, G. Ceder, A. Jain, M. Asta, A. Gamst, A statistical learning framework for materials science: application to elastic moduli of k-nary inorganic polycrystalline compounds, *Scientific Reports* 6 (September) (2016) 34256, doi:10.1038/srep34256.
- [66] E. Clouet, M. Nastar, C. Sigli, Nucleation of Al<sub>3</sub>Zr and Al<sub>3</sub>Sc in aluminum alloys: From kinetic Monte Carlo simulations to classical theory, *Physical Review B* 69 (6) (2004) 064109.
- [67] S. Shu, P. Wells, N. Almirall, G. Odette, D. Morgan, Thermodynamics and kinetics of core-shell versus appendage co-precipitation morphologies: An example in the Fe-Cu-Mn-Ni-Si system, *Acta Materialia* 157 (2018) 298–306.
- [68] F. Mouhat, F. Coudert, Necessary and sufficient elastic stability conditions in various crystal systems, *Physical review B* 90 (22) (2014) 224104.
- [69] A. Van De Walle, Q. Hong, S. Kadhodaei, R. Sun, The free energy of mechanically unstable phases, *Nature communications* 6 (1) (2015) 1–6.
- [70] S. Kadhodaei, Q. Hong, A. van de Walle, Free energy calculation of mechanically unstable but dynamically stabilized bcc titanium, *Physical Review B* 95 (6) (2017) 064101.
- [71] S. Kadhodaei, A. van de Walle, Software tools for thermodynamic calculation of mechanically unstable phases from first-principles data, *Computer Physics Communications* 246 (2020) 106712.
- [72] C. Loader, Local regression and likelihood, Springer Science & Business Media, 2006.
- [73] Y. Hu, G. Zhao, M. Zhang, B. Bin, T. Del Rose, Q. Zhao, Q. Zu, Y. Chen, X. Sun, M. de Jong, L. Qi, Predicting densities and elastic moduli of SiO<sub>2</sub>-based glasses by machine learning, *npj Computational Materials* 6 (1) (2020) 1–13.
- [74] Y. Hu, M. Fellingner, B. Butler, Y. Wang, K. Darling, L. Kecskes, D. Trinkle, Z. Liu, Solute-induced solid-solution softening and hardening in bcc tungsten, *Acta Materialia* 141 (2017) 304–316.
- [75] N. Al-Zoubi, S. Schönecker, X. Li, W. Li, B. Johansson, L. Vitos, Elastic properties of 4d transition metal alloys: Values and trends, *Computational materials science* 159 (2019) 273–280.
- [76] C. Ren, Z. Fang, M. Koopman, B. Butler, J. Paramore, S. Middlemas, Methods for improving ductility of tungsten—a review, *International Journal of Refractory Metals and Hard Materials* 75 (2018) 170–183.
- [77] W. Klopp, Review of ductilizing of group VIA elements by rhenium and other solutes, 4955, National Aeronautics and Space Administration, 1968.
- [78] Y. Tong, S. Zhao, H. Bei, T. Egami, Y. Zhang, F. Zhang, Severe local lattice distortion in Zr-and/or Hf-containing refractory multi-principal element alloys, *Acta Materialia* 183 (2020) 172–181.
- [79] J. Zhang, Y. Hu, Q. Wei, Y. Xiao, P. Chen, G. Luo, Q. Shen, Microstructure and mechanical properties of RexNbMoTaW high-entropy alloys prepared by arc melting using metal powders, *Journal of Alloys and Compounds* 827 (2020) 154301.
- [80] E. Rappaport, M. Smith, The constitution diagram Tungsten-Ruthenium, *Transactions of the Metallurgical Society of AIME* 230 (1964) 6–11.
- [81] R. Mathieu, N. Dupin, J.-C. Crivello, K. Yaqoob, A. Breidi, J.-M. Fiorani, N. David, J.-M. Joubert, CALPHAD description of the Mo-Re system focused on the sigma phase modeling, *Calphad* 43 (2013) 18–31.
- [82] X. Liu, C. Hargather, Z. Liu, First-principles aided thermodynamic modeling of the Nb-Re system, *Calphad* 41 (2013) 119–127.
- [83] H. Yao, J. Qiao, G. MC, J. Hawk, S. Ma, H. Zhou, Y. Zhang, NbTaV-(Ti,W) refractory high-entropy alloys: Experiments and modeling, *Materials Science and Engineering: A* 674 (2016) 203–211, doi:10.1016/j.msea.2016.07.102.
- [84] Y. Zhang, X. Yang, P. Liaw, Alloy design and properties optimization of high-entropy alloys, *Jom* 64 (7) (2012) 830–838.
- [85] X. Yang, Y. Zhang, P. Liaw, Microstructure and compressive properties of NbTiVAlx high entropy alloys, *Procedia Engineering* 36 (2012) 292–298.
- [86] O. Senkov, S. Senkova, C. Woodward, D. Miracle, Low-density, refractory multi-principal element alloys of the Cr-Nb-Ti-V-Zr system: Microstructure and phase analysis, *Acta Materialia* 61 (5) (2013) 1545–1557.
- [87] Y. Wu, Y. Cai, T. Wang, J. Si, J. Zhu, Y. Wang, X. Hui, A refractory Hf<sub>2</sub>Nb<sub>2</sub>Si<sub>2</sub>Ti<sub>2</sub>W<sub>2</sub> high-entropy alloy with excellent structural stability and tensile properties, *Materials Letters* 130 (2014) 277–280.
- [88] Z. Liu, First-principles calculations and CALPHAD modeling of thermodynamics, *Journal of phase equilibria and diffusion* 30 (5) (2009) 517.
- [89] D. Miracle, J. Miller, O. Senkov, C. Woodward, M. Uchic, J. Tiley, Exploration and development of high entropy alloys for structural applications, *Entropy* 16 (1) (2014) 494–525.
- [90] Z. Pei, J. Yin, J. Hawk, D. Alman, M. Gao, Machine-learning informed prediction of high-entropy solid solution formation: Beyond the Hume-Rothery rules, *npj Computational Materials* 6 (1) (2020) 1–8.
- [91] Z. Zhou, Y. Zhou, Q. He, Z. Ding, F. Li, Y. Yang, Machine learning guided appraisal and exploration of phase design for high entropy alloys, *npj Computational Materials* 5 (1) (2019) 1–9.
- [92] W. Huang, P. Martin, H. Zhuang, Machine-learning phase prediction of high-entropy alloys, *Acta Materialia* 169 (2019) 225–236.
- [93] C. Niu, Y. Rao, W. Windl, M. Ghazisaeidi, Multi-cell Monte Carlo method for phase prediction, *npj Computational Materials* 5 (1) (2019) 120.
- [94] E. Antillon, M. Ghazisaeidi, Efficient determination of solid-state phase equilibrium with the multicell Monte Carlo method, *Physical Review E* 101 (6) (2020) 063306.
- [95] A. Natarajan, A. Van der Ven, Machine-learning the configurational energy of multicomponent crystalline solids, *npj Computational Materials* 4 (1) (2018) 1–7.
- [96] S. Wei, S. Kim, J. Kang, Y. Zhang, Y. Zhang, T. Furuhashi, E. Park, C. Tatan, Natural-mixing guided design of refractory high-entropy alloys with as-cast tensile ductility, *Nature Materials* 19 (11) (2020) 1175–1181, doi:10.1038/s41563-020-0750-4.
- [97] O. Senkov, S. Semiatin, Microstructure and properties of a refractory high-entropy alloy after cold working, *Journal of Alloys and Compounds* 649 (2015) 1110–1123, doi:10.1016/j.jallcom.2015.07.209.
- [98] O. Senkov, G. Wilks, J. Scott, D. Miracle, Mechanical properties of Nb<sub>25</sub>Mo<sub>25</sub>Ta<sub>25</sub>W<sub>25</sub> and V<sub>20</sub>Nb<sub>20</sub>Mo<sub>20</sub>Ta<sub>20</sub>W<sub>20</sub> refractory high entropy alloys, *Intermetallics* 19 (5) (2011) 698–706, doi:10.1016/j.intermet.2011.01.004.
- [99] B. K. J. L. H. JR, S. HH, Ultra-high strength WNbMoTaV high-entropy alloys with fine grain structure fabricated by powder metallurgical process, *Materials Science and Engineering: A* 712 (2018) 616–624, doi:10.1016/j.msea.2017.12.021.
- [100] N. Guo, L. Wang, L. Luo, X. Li, R. Chen, Y. Su, J. Guo, H. Fu, Microstructure and mechanical properties of in-situ MC-carbide particulates-reinforced refractory high-entropy Mo<sub>0.5</sub>NbHf<sub>0.5</sub>ZrTi matrix alloy composite, *Intermetallics* 69 (2016) 74–77, doi:10.1016/j.intermet.2015.09.011.
- [101] Effect of Ti additions on mechanical properties of NbMoTaW and VNbMoTaW refractory high entropy alloys, *Intermetallics* 84 (2017) 153–157, doi:10.1016/j.intermet.2017.01.007.
- [102] Y. Wu, Y. Cai, X. Chen, T. Wang, J. Si, L. Wang, Y. Wang, X. Hui, Phase composition and solid solution strengthening effect in TiZrNbMoV high-entropy alloys, *Materials & Design* 83 (2015) 651–660, doi:10.1016/j.matdes.2015.06.072.
- [103] N. Guo, L. Wang, L. Luo, X. Li, Y. Su, J. Guo, H. Fu, Microstructure and mechanical properties of refractory MoNbHfZrTi high-entropy alloy, *Materials & Design* 81 (2015) 87–94.
- [104] S. Maiti, W. Steurer, Structural-disorder and its effect on mechanical properties in single-phase TaNbHfZr high-entropy alloy, *Acta Materialia* 106 (2016) 87–97, doi:10.1016/j.actamat.2016.01.018.
- [105] Z. Han, H. Luan, X. Liu, N. Chen, X. Li, Y. Shao, K. Yao, Microstructures and mechanical properties of TiNbMoTaW refractory high-entropy alloys, *Materials Science and Engineering: A* 712 (2018) 380–385, doi:10.1016/j.msea.2017.12.004.
- [106] N. Guo, L. Wang, L. Luo, X. Li, R. Chen, Y. Su, J. Guo, H. Fu, Effect of composing element on microstructure and mechanical properties in Mo-Nb-Hf-Zr-Ti multi-principle component alloys, *Intermetallics* 69 (2016) 13–20, doi:10.1016/j.intermet.2015.10.011.
- [107] O. Senkov, J. Scott, S. Senkova, D. Miracle, C. Woodward, Microstructure and room temperature properties of a high-entropy TaNbHfZrTi alloy, *Journal of Alloys and Compounds* 509 (20) (2011) 6043–6048, doi:10.1016/j.jallcom.2011.02.171.
- [108] C.-C. Juan, K.-K. Tseng, W.-L. Hsu, M.-H. Tsai, C.-W. Tsai, C.-M. Lin, S.-K. Chen, S.-J. Lin, J.-W. Yeh, Solution strengthening of ductile refractory HfMoNbTaTiZr high-entropy alloys, *Materials Letters* 175 (2016) 284–287, doi:10.1016/j.matlet.2016.03.133.
- [109] S. Chen, X. Yang, K. Dahmen, P. Liaw, Y. Zhang, Microstructures and crackling noise of AlxNbTiMoV high entropy alloys, *Entropy* 16 (2) (2014) 870–884.
- [110] E. Fazakas, V. Zadorozhnyy, L. Varga, A. Inoue, D. Louzguine-Luzgin, F. Tian, L. Vitos, Experimental and theoretical study of Ti<sub>20</sub>Zr<sub>20</sub>Hf<sub>20</sub>Nb<sub>20</sub>X<sub>20</sub> (X= V or Cr) refractory high-entropy alloys, *International Journal of Refractory Metals and Hard Materials* 47 (2014) 131–138.
- [111] Y. Zou, S. Maiti, W. Steurer, R. Spolenak, Size-dependent plasticity in an Nb<sub>25</sub>Mo<sub>25</sub>Ta<sub>25</sub>W<sub>25</sub> refractory high-entropy alloy, *Acta Materialia* 65 (2014) 85–97, doi:10.1016/j.actamat.2013.11.049.
- [112] Y. Zou, P. Okle, H. Yu, T. Sumigawa, T. Kitamura, S. Maiti, W. Steurer, R. Spolenak, Fracture properties of a refractory high-entropy alloy: In situ micro-tensile and atom probe tomography studies, *Scripta Materialia* 128 (2017) 95–99, doi:10.1016/j.scriptamat.2016.09.036.
- [113] J. Bao, L. Gagliardi, D. Truhlar, Self-Interaction Error in Density Functional Theory: An Appraisal, *The Journal of Physical Chemistry Letters* 9 (9) (2018) 2353–2358.
- [114] A. Patra, J. Bates, J. Sun, J. Perdew, Properties of real metallic surfaces: Effects of density functional semilocality and van der Waals nonlocality, *Proceedings of the National Academy of Sciences* 114 (44) (2017) E9188–E9196, doi:10.1073/pnas.1713320114.
- [115] P. Lazar, M. Otyepka, Accurate surface energies from first principles, *Phys. Rev. B* 91 (2015) 115402, doi:10.1103/PhysRevB.91.115402.
- [116] P. Lazar, J. Martincová, M. Otyepka, Structure, dynamical stability, and electronic properties of phases in Ta<sub>2</sub> from a high-level quantum mechanical calculation, *Phys. Rev. B* 92 (2015) 224104, doi:10.1103/PhysRevB.92.224104.
- [117] E. Mak, B. Yin, W.A. Curtin, A ductility criterion for bcc highentropy alloys, *J. Mech. Phys. Solids* (2021), doi:10.1016/j.jmps.2021.104389.